UNIVERSITAT POLITÈCNICA DE VALÈNCIA

DEPARTAMENT DE COMUNICACIONS

Integrated spectroscopic sensor fabricated in a novel Si_3N_4 platform

Ph.D. THESIS

by
Gloria Micó Cabanes

Ph.D. Supervisors:
Dr. Pascual Muñoz Muñoz
Dr. Daniel Pastor Abellán

Valencia, July 2020

UNIVERSITAT POLITÈCNICA DE VALÈNCIA

DEPARTAMENT DE COMUNICACIONS

Integrated spectroscopic sensor fabricated in a novel Si_3N_4 platform

Gloria Micó Cabanes
Photonics Research Labs
ITEAM Research Institute
Universitat Politècnica de València
Camí de Vera s/n, 46022 Valencia, SPAIN
glomica@iteam.upv.es

Ph.D. Supervisors:
Dr. Pascual Muñoz Muñoz
Dr. Daniel Pastor Abellán

Valencia, July 2020

A mi familia

"Nothing in this world should be feared, only understood.
Now is the time to understand more, so that we may fear less."

"Nada en este mundo debe ser temido, sólo entendido.
Ahora es el momento de entender más, para que podamos temer menos."

Marie Curie

Agradecimientos

Han sido muchas las personas que me han acompañado en este recorrido y a las que quiero agradecer su apoyo.

Los primeros en la lista son, por supuesto, mis tutores. Pascual Muñoz y Daniel Pastor, quiero daros las gracias a ambos por introducirme en el mundo de la fotónica integrada y brindarme la oportunidad de desarrollar esta tesis. Gracias por compartir vuestros conocimientos conmigo, por vuestra paciencia, y por todo el apoyo que me habéis demostrado durante este proceso. Me habéis ayudado a hacer esto posible.

Quiero agradecer también a las dos personas que me iniciaron en la parte más práctica del trabajo el tiempo que me dedicaron. A Rocío Baños, por enseñarme a desenvolverme en el laboratorio; porque gran parte de lo que sé te lo debo a ti y a todas las horas que compartimos delante de los setups. Y a Bernardo Gargallo, por ayudarme con las primeras simulaciones y darme la base con la que he desarrollado el trabajo de esta tesis. Dentro del equipo de VLC Photonics, no puedo olvidarme de David Domenech y Juan Fernández, que habéis estado siempre disponibles para cualquier consulta, tanto en temas de laboratorio como de diseño.

Me gustaría dar las gracias a Carlos Domínguez y a todo el equipo del CNM, por servirme de guía en todo lo referente a la fabricación de PICs y por la confianza y accesibilidad que me demostrastéis desde el primer momento.

Quiero agradecer a todos los miembros del antiguo GCOC y nuevo PRL con los que me he cruzado en esta andadura, todos los momentos compartidos a lo largo de estos años: miles de anécdotas a la hora de la comida, opiniones diversas, recomendaciones de series, viajes a congresos y alguna que otra cerveza... Ha sido toda una suerte poder formar parte de este grupo y estar rodeada de tan buena gente. Quiero hacer una mención especial aquí a Luis, Jesús y Dani, que os habéis convertido en mi familia del trabajo. Gracias de corazón por todas las risas dentro y fuera de la universidad, por nuestros momentos de terapia y por vuestra amistad, que es de las mejores cosas que me ha aportado este doctorado.

Y por último, quiero dar las gracias a toda mi familia por el apoyo y cariño que me habéis mostrado tanto en esta etapa, como a lo largo de toda mi vida. Gracias a mi padre y a mi madre por vuestra confianza, vuestro amor infinito y vuestra fe ciega en mi. Y cómo no, a mi compañero de vida, Alex, que has sido un pilar fundamental, ayudándome a sobrellevar los momentos duros y celebrando todos mis éxitos. Gracias a todos por estar siempre a mi lado.

Abstract

This thesis is focused on the model, design and experimental demonstration of an integrated spectroscopic sensor based on a modified Arrayed Waveguide Grating (AWG). The device has been designed and fabricated in a new silicon nitride (Si_3N_4) on silicon oxide (SiO_2) platform developed in Spain. The work performed for this thesis can be then divided into two main sections. In the first part, an overview of the existing Si_3N_4 platforms and their state of art is described, alongside the report on the fabrication and characterization of our 300 nm guiding film height Si_3N_4 platform. On the second part, the device named Integrated Optical Spectroscopic Sensor (IOSS) is presented. The IOSS consists of an AWG which arrayed waveguides are divided into two sub-sets engineered to replicate the AWG channels. The waveguides of one of the sub-sets contain sensing windows, defined as waveguides sections which core is in contact with the surrounding media. Thus, the sensing is performed through evanescent field interaction with the sample deposited. The waveguides from the second sub-set remain isolated. Therefore, the device provides both sensing and reference spectra. The IOSS mathematical model, design procedure and proof of concept configured for absorption spectroscopy are reported in this thesis.

Resumen

Esta tesis se ha centrado en el modelado, diseño y demostración experimental de un sensor espectroscópico integrado basado en un AWG (del inglés *Arrayed Waveguide Grating*). El dispositivo ha sido diseñado y fabricado en una nueva plataforma de nitruro de silico (Si_3N_4) en oxido de silico (SiO_2) desarrollada en España. El trabajo realizado en esta tesis se puede dividir en dos secciones principalmente. En la primera parte, se describe el panorama general de las plataformas de Si_3N_4 existentes y su estado del arte, junto con la descripción de los procesos de fabricación y caracterización de nuestra plataforma de Si_3N_4 con 300 nm de altura en la capa de guiado. En la segunda parte, se presenta el dispositivo bautizado como *Integrated Optical Spectroscopic Sensor* (IOSS). El IOSS consiste en un AWG cuyos conjunto de guías de onda está dividido en dos subgupos diseãdos para replicar los canales del AWG. Las guías de uno de los subgrupos contiene ventanas de sensado, que están definidas por secciones en las que el núcleo de las guías está al descubierto y, por tanto, en contacto con el medio que las rodea. De esta manera, el sensado se lleva a cabo mediante la interacción del campo evanescente con la muestra depositada. Las guías del segundo subconjunto permanecen inalteradas. Por lo tanto, el dispositivo proporciona al mismo tiempo los espectros de sensado y de referencia. El modelo matemático del IOSS, su procedimiento de diseño y la prueba de concepto del sensor configurado para espectroscopía de absorción se describen en esta tesis.

Resum

La present tesi s'ha centrat en el modelatge, disseny i demostració experimental d'un sensor espectroscòpic integrat basat en un AWG (de l'anglès *Arrayed Waveguide Grating*). El dispositiu ha sigut dissenyat i fabricat en una nova plataforma de nitrur de silici (Si_3N_4) en òxid de silici (SiO_2) desenvolupada a Espanya. El treball realitzat en aquesta tesi es pot dividir en dues seccions principalment. En la primera part, es descriu el panorama general de les plataformes de Si_3N_4 existents i el seu estat de l'art, juntament amb la descripció dels processos de fabricació i caracterització de la nostra plataforma de Si_3N_4 amb 300 nm d'altura en la capa de guiat. En la segona part, es presenta el dispositiu batejat com *Integrated Optical Spectroscopic Sensor* (IOSS). El IOSS consisteix en un AWG en el que el seu el conjunt de guies d'ona està dividit en dos subgrups dissenyats per a replicar els canals del AWG. Les guies d'un dels subgrups conté finestres de detecció, que estan definides per seccions en les quals el nucli de les guies d'ona està al descobert i en contacte amb el mitjà que li envolta. D'aquesta manera, la detecció es duu a terme mitjançant la interacció del camp evanescent amb la mostra depositada. Les guies del segon subconjunt romanen inalterades. Per tant, el dispositiu proporciona al mateix temps els espectres de detecció de referència. El model matemàtic del IOSS, el seu procediment de disseny i la prova de concepte del sensor configurat per a espectroscopia d'absorció es descriuen en aquesta tesi.

Contents

List of Figures

List of Tables

Chapter 1
Introduction

Although optics is a science that has been studied since ancient times, in the last sixty years there have been key developments that have made the field evolve significantly. The invention of the laser by Maiman in 1960 [2], the development of semiconductors optical devices (as laser diodes and photo-detectors) by Holonyak an Riesz in 1962 [3], or the fabrication of very cheap optical fibers with low propagation losses by Kao and Hockham in the 1970s [4], are some of the most relevant examples. The undergoing optics evolution required a term in which light is treated in terms of photons, given the relevance of the interaction of light with matter (from the point of view of the devices named above). Therefore, the term "photonics" became known in conjunction with the invention of these devices.

Photonics is then the science and technology dealing with the generation, detection and manipulation of light over the whole spectrum, from ultraviolet, over visible through the near, mid and part of the far infrared (0.4-30 μm in wavelength). It is considered on of the key technologies in the 21st century due to the high impact it has had in multiple fields as telecommunications, health care and life sciences, security, defence, lighting and illumination, optical metrology or sensing, among others.

Within the field of photonics, the branch of integrated photonics basically arose from the idea of using photons instead of electrons, creating integrated optical circuits similar to those in conventional electronics. The term *integrated optics* was first coined by S. Miller [5] in 1969, and since then, a lot of effort has been put in the study and development of several integrated technologies based on different materials combinations [6]. The implementation of multiple functionalities in a single photonic circuit makes integrated photonics a very promising technology.

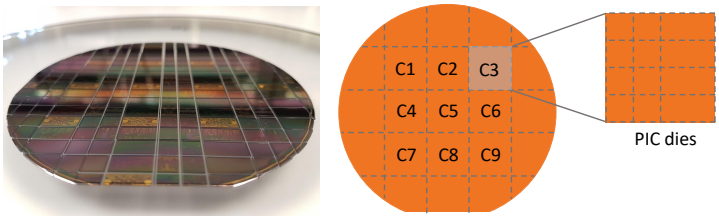

Figure 1.1: Picture of an already diced 4 inch wafer of a CNM-VLC MPW run (left) and an scheme of its cells/dies definition (right).

1.1 Integrated photonics platforms

Photonic integrated circuits (PICs) technology is becoming more and more standardized and reachable thanks to the generic manufacturing processes that have been developed, and their access through multi-project wafer (MPW) runs [1]. MPW runs offer the opportunity to share design space on the same wafer between several users. Thus, the total production expense is reduced by dividing the costs of the mask and the fabrication process among the customers. The wafer design area is divided into several replicated sections (reticles number and size may change between platforms), and then diced into the final PIC dies (Figure 1.1).

Among all the amenable materials to produce PICs, the main three employed in generic integration platforms are Silicon on Insulator (SOI) [7], Indium Phosphide (InP) [8] and Silicon Nitride (SiNx) [9]. Each of these materials is transparent in a determined wavelength range, as shown in Figure 1.2, where the main photonics applications (biophotonics, tele/datacom, and sensing) and their operating range in wavelength are also depicted. Therefore, each application requires the use of a specific material. As can be observed from Figure 1.2, III-V semiconductors (such as InP, InAs, GaAs, GaN, AlGaAs, InGaAsP or InSb) are employed for NIR applications, for which SOI material can be also used. The choice of using III-V or SOI material is mainly given by the need to implement or not active elements, as lasers, in the design. In turn, silicon nitride on silicon oxide is transparent in a wider wavelength range (from visible to upper part of mid infrared). Technologies employing SiO_2 are limited in the upper part of the spectrum to approximately 4 μm, which is due to the strong absorption that this material presents from that point forward. For applications working in the NIR-MIR, other materials combination are employed, as for example, germanium on silicon [10–14].

InP is the only technology allowing for monolithic integration of active devices including lasers, semiconductor optical amplifiers (SOAs), photodetectors and modulators, whith passive components [15,16]. It is considered to be a moderate optical confinement technology, therefore the compactness of the devices as well as the integration density are low. Foundries offering MPW runs in this technology are Fraunhofer HHI [17] and SmartPhotonics [18] SOI is a semiconductor technology with high index contrast [7], resulting in small footprint circuits and

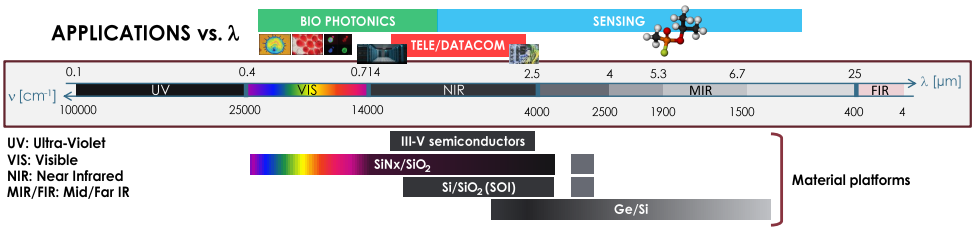

Figure 1.2: Applications versus wavelength range, and the different material systems, III–V semiconductor and Silicon photonics, commonly employed in generic photonic integration (Reference [1], adapted with permission from OSA Publishing).

high integration density on chip. The main advantage of this technology lies in its compatibility with CMOS fabrication processes. On the contrary, the main drawbacks of this high optical confinement technology are the phase errors and propagation losses due to the interaction of the propagating mode with the sidewall roughness. In addition, no optical sources or optical amplifiers can be implemented, and the Pockels effect is poor, thus it is also not possible to implement electro-optic efficient modulators. This, however, can be solved by integrating III-V functionalities into the SOI platform [23], although this implies additional fabrication steps. Some expamles of foundries offering SOI MPW runs are imec, X-FAB, STMicroelectronics or GlobalFoundries. All these platforms are offered by Europractice-IC broker [19].

Finally, SiNx technology is a dielectric based photonic technology which operates in a wide wavelength range, going from visible to mid infrared, with very low loss [24]. This is a purely passive technology, therefore no optical sources, detectors, amplifiers or modulators are availabe in the generic MPW processes. However, common integration of these components can be achieve thourgh hybrid or heterogeneous approaches with separately fabricated InP or Si PICs. Foundries offering SiNx MPW runs are LioniX (TriPleX^{TM} technology) [20], LIGENTEC [21], and for five years now, CNM-VLC foundry [22], in which we are working on.

This thesis is focused on the characterization and sensing applications on the moderate confinement Si_3N_4/SiO_2 waveguide platform developed by CNM-VLC, amenable for applications from the VIS to the long NIR (400–3700 nm wavelength range).

1.2 Silicon Nitride Platforms: State of the art.

In microelectronics, Si_3N_4 material is widely employed as a passivation layer and chemical barrier in integrated circuits, as well as complementary dielectric material to implement extra components due to its electrical, thermal and chemical features [25]. In the field of photonics, the first fabrication of Si_3N_4 films on a SiO_2 buffer

on Silicon wafers operating at 632 nm was reported by Stulius and Streifer in 1977 [26]. In the following years, several works were performed in the visible spectrum range employing straight Si_3N_4 waveguides, being a seminal contribution the device presented by Heideman E.A. [27] in 1993. It was a partially integrated Mach-Zehnder Interferometer (MZI) employed for immunosensing assays, in which both arms were Si_3N_4/SiO_2 waveguides, whereas the optical couplers were external to the photonic chip. A fully integrated MZI was presented four years later [28]. The interest in this technology went further in 2005, when new developed processes and applications were developed in the near infrared (NIR) [29, 30]. From 2008 to 2011, silicon oxynitride (SiONx) waveguides [31] and Si_3N_4 waveguides [32–34] were reported working in this same spectrum range. Most of the applications operating in the NIR were presented for telecom related groups, which working range of interest in wavelength is in the C-band (1550 nm). For this reason, all the waveguide cross-sections were engined for moderate confinement (film heights $>$ 100 nm), although in 2011, low confinement waveguides were also published (film heights $<$ 100 nm) [33]. Two years later, by 2013, researchers had implemented new configurations of Si_3N_4 technology for VIS applications [35, 36]. Meanwhile, high confinement waveguides (film heights $>$ 400 nm) started to become more relevant for the long NIR (NIR+) (wavelength $>$ 2000 nm) [37–40]. In recent years, they have emerged new contributions in moderate confinement techniques [41–43].

In Table 1.1 have been compiled all the strip silicon nitride waveguides published in literature. The table collates information on the operation wavelength, layer stack, cross-section dimensions, and when available, cut-off wavelength, propagation loss and bend radius. The main factors causing optical propagation loss are two [29]: i) the surface roughness (film roughness and waveguide sidewall roughness), and ii) the mode confinement, which depends on the operating wavelength, waveguide core cross-section, as well as height and material of the layers around it. Hence, propagation losses will be lower either when the propagating mode is highly confined or the sidewall roughness is minimum.

The strip waveguides presented in Table 1.1 can be categorized in three groups depending on their working spectrum range and optical confinement. The characteristics of each strip waveguide group are discussed bellow, focusing on the NIR range. However, it is worth noting the relevance of other types of waveguides reported in [44–46], as are box waveguide and double strip waveguide (Figure 2.1, BOXWVG and DSWVG respectively), with propagation loss and bend radius as low as 0.1 dB/cm and 70 μm.

Low confinement waveguides were reported by Lionix and UCSB. The core cross-section were $\sim$100 nm height by $\sim$2800 nm width, and they presented propagation losses as low as 0.09 dB/cm at 1550 nm for 0.5 mm bend radius, being 0.001 dB/cm the lowest loss demonstrated by these groups. Such low losses are due to the fact that the mode is mostly propagated through the cladding and the sidewall roughness is minimized,which is achieved by the large heights of cladding and buried oxide (BOX) layers (7.5 μm and 8 μm respectively).

When the nitride layer height is between 150 and 400 nm, waveguides are classified as moderate confinement waveguides. Several groups have characterised

the operation of such waveguides in the NIR. Sandia [29] and UCD [42] reported LPCVD Si_3N_4 guiding film heights of ∼150–200 nm, with waveguide widths ∼800–2000 nm. They achieve 0.11–1.45 dB/cm propagation loss for BOX height up to 5.0 μm. 3D SiNx on top of SOI working in the NIR are reported by IME and University Toronto [47], employing LPCVD Si_3N_4 guiding film heights ∼300–400 nm, with waveguide widths ∼800–1000 nm, resulting into propagation loss of 1.30–2.10 dB/cm at 1550 nm for BOX heights in between 2.0 μm and 5.0 μm. On the other hand, moderate confinement waveguides have been also reported in the VIS range employing similar film heights. University Aachen and University Gent reported PECVD guiding film heights ∼100–220 nm, waveguide widths ∼300–800 nm PECVD guiding film loss 0.51–2.25 dB/cm at 532–600 nm for BOX height ∼2400 nm.

For the case of high confinement waveguides, several groups have reported works in the NIR and NIR+ : Kippengerg (EPFL) [37], Lipson (Cornell, then Columbia) [38, 40, 48] and Agarwal (MIT) in 2013 [49], followed in 2015 by Torres (Chalmers) [39] and companies such as LioniX [24] and LigenTec [50].These waveguides are characterized by core heights between ∼700 and 2500 nm, and widths going from ∼700 to 4000 nm. The propagation losses reported for BOX heights in the range of 2.0–8.0 μm are 0.04–1.37 dB/cm measured at 1550 nm, and 0.16–2.1 dB/cm at 2600–3700 nm.

Group	Range	λ (nm)	Substrate	Core	Cladding	Confinement	Width (nm)	Height (nm)	Cut-off λ (nm) @ Width (nm)	Bend R (μm)	Straight (dB/cm) @ λ (nm)
Gent/Baets [36]	VIS	532	SiO_2 (h = 2.0 μm) HDP-CVD	SiN PECVD	SiO_2 (h = 2.0 μm)	Moderate	300 400 500	180	530 @ 532		7.00 @ 532 3.25 @ 532 2.25 @ 532
Aachen/Witzens [35]	VIS	660	SiO_2/ 1.45 (h = ?)	SiN / 1.87 PECVD	SiO_2 (Water)	Moderate	700	100	580	35 (60)	0.51 @ 600 (0.71)
Gent/Baets [36]	VIS+	780	SiO_2 (h = 2.4 μm) HDP-CVD	SiN PECVD 1.89@780	SiO_2 (h = 2.0 μm)	Moderate	500 600 700	220	900 @ 780		2.25 @ 780 1.50 @ 780 1.30 @ 780
Gent/Baets [36]	VIS+	900	SiO_2 (h = 2.4 μm)HDP-CVD	SiN PECVD	SiO_2 (h = 2.0 μm)	Moderate	600 700 800	220	1100 @ 900		1.30 @ 900 0.90 @ 900 0.62 @ 900
IME/Lo [51]	NIR	1270–1580	SiO_2 (h = 2.2 μm)	Si_3N_4 LPCVD	SiO_2	Moderate	1000	400			0.32 @ 1270 1.30 @ 1550 0.40 @ 1580
IME/Lo [51]	NIR	1270–1580	SiO_2 (h = 3.32 μm)	Si_3N_4 PECVD	SiO_2	Moderate	1000	400			0.45 @ 1270 3.75 @ 1550 1.10 @ 1580
IME/Lo [51]	NIR	1270–1580	SiO_2 (h = 3.32 μm)	Si_3N_4 PECVD	SiO_2	Moderate	1000	600			0.24 @ 1270 3.50 @ 1550 0.80 @ 1580
Trento/Pavesi [30]	NIR	1550	SiO_2 (h = 2.5 μm)	Multi-layer	Air / SiO_2	Moderate					1.50 @ 1550 nm
Sandia/Sullivan [29]	NIR	1550	SiO_2 (h = 5.0 μm)	Si_3N_4 LPCVD	SiO_2 (h = 4.0 μm) PECVD or HDP	Moderate	800	150		500	0.11–1.45 @ 1550
Twente/Driesen [31]	NIR	1550	SiO_2/ 1.45 (h = ?)	SiON PECVD	?	Moderate	2000–2500	140–190		25–50	0.20 @ 633 0.20 @ 1550
IME/Lo [32]	NIR	1550	SiO_2 (h = 5.0 μm) PECVD	SiN / 2.03 (h = 400nm) PECVD	SiO_2 (h = 2.0 μm) PECVD	Moderate	700	400			2.1 @ 1550
LioniX-UCSB [33, 34]	NIR	1550	SiO_2/ 1.45 (h = 8.0 μm)	Si_3N_4 LPCVD	SiO_2/ 1.45 (h = 7.5 μm)	Low	2800	100		500	0.09 @ 1550
LioniX-UCSB [33, 34]	NIR	1550	SiO_2/ 1.45 (h = 8.0 μm)	Si_3N_4 LPCVD	SiO_2/ 1.45 (h = 7.5 μm)	Low	2800	80		2000	0.02 @ 1550
Cornell/Lipson [48]	NIR	1550	SiO_2 (h = 4 μm)	Si_3N_4 LPCVD	SiO_2 (500 nm + 2.5 μm)	High	2500	730		115	0.008 @ 1550
LioniX [24]	NIR	1550	SiO_2 (h = 8.0 μm)	Si_3N_4 LPCVD	SiO_2 (h = 8.0 μm)	High	700-900	800 1000 1200			0.37 @ 1550 0.45 @ 1550 1.37 @ 1550
Toronto-IME/Poon [47]	NIR	1270–1580	SiO_2 (h = 2.2 μm)	Si_3N_4 LPCVD	SiO_2	Moderate	900	400			0.34 @ 1270 1.30 @ 1550 0.40 @ 1580
Toronto-IME/Poon [47]	NIR	1270–1580	SiO_2 (h = 3.32 μm)	SixNy PECVD	SiO_2	Moderate	1000	600			0.24 @ 1270 3.50 @ 1550 0.80 @ 1580
CNM-VLC	NIR	1550	SiO_2 (h = 2.5 μm)	Si_3N_4 LPCVD	SiO_2 (1.50 μm)	Moderate	1000	300		150	1.41 @ 1550
UCD/Yoo [42]	NIR	1550	SiO_2 (h = ?)	Si_3N_4 LPCVD	SiO_2 (h = 2.0 μm)	Moderate	2000	200		50	0.30 @ 1550
LigenTec [50]	NIR	1550	SiO_2 (0.13–3.5 μm) Thermal	Si_3N_4 LPCVD	SiO_2	High	2000	800		119	?
Chalmers/Torres [39]	NIR	1550	SiO_2 (h = 2.0 μm)	Si rich SiNx LPCVD	SiO_2 (h = 2.0 μm)	High	1650	700		20	1.00 @ 1550
Wang/Gent [52]	NIR	1550	SiO_2 (h = 5.0 μm)	SiN PECVD	SiO_2 (h = 3.0 μm)	High	1200 2000	580		100	1.27 @ 1550 0.58 @ 1550
Ghuagzhou/Shao [53]	NIR	1550–1600	SiO_2 (h = 2.0 μm)	SixNy ICP-CVD	?	Moderate	1400	600		40	0.79 @ 1575
Columbia/Lipson [38]	NIR+	2300–3500	SiO_2 (h = 4.5 μm)	Si_3N_4 LPCVD	SiO_2 (500 nm + 2 μm)	High	2700	950	2500	230	0.60 @ 2600
MIT/Agarwal [49, 54]	NIR+	2400–3700	SiO_2/ 1.45 (h = 4 μm)	Si rich SiNx LPCVD	SiO_2	High	4000	2500		200 @ 2650 200 @ 3700	0.16 @ 2650 2.10 @ 3700

Table 1.1: State of the art of silicon nitride strip waveguide platforms.

1.3 Integrated sensors

Among the different photonic integrated circuits (PIC) applications, on-chip photonic sensors have generated increasing interest in recent decades, since the early 1980s [55]. The growing popularity of optical sensors was due to their high sensitivity, fast response and the possibility to perform real-time measurements [56]. These features were enhanced when optical sensors were implemented as integrated devices, as this provides, in addition to the characteristics mentioned above, robustness, reliability, miniaturization and the possibility of mass production.

As it was explained in previous section, Silicon Nitride on Silicon Oxide technology platforms operate along a broad wavelength range, from visible to the mid-infrared (400-3700 nm). This is an interesting spectrum range, from a light-matter interaction perspective, since electronic transitions and molecular vibrations show emission/absorption peaks in this range. Moreover, the chemical, mechanical and thermal stability characteristics of Si_3N_4 technology [57] make it the most appropriate platform for bio/chemical and medical sensing purposes. In recent years, various optical applications have been published employing Si_3N_4 PICs, as for example, super-resolution microscopy, labelled and label-free bio-sensors, cytometry or OCT, to name a few [58].

For these applications, diverse optical measurement techniques are employed such fluorescence, refractometry, emission, absorption or polarimetry, as reported in [59]. The main employed detection technique in optical (bio/chemical)-sensors is the evanescent field sensing [59]. This technique analyses the variation of the propagation optical properties (i.e. refractive index) due to the interaction of the evanescent field of the device with the sample under study. The analysis may be perform either on the real part (frequency/wavelength interrogation) or the imaginary part (intensity interrogation) of the refractive index. This kind of detection and interrogation methods are employed in Surface Plasmon Resonance (SPR) sensors [60] and sensors based on planar waveguides, where the core of the waveguide is in direct contact with the sample. For the latter, diverse architectures have been applied as: Bi-modal Waveguides (BiWG) [61], Mach-Zehnder Interferometers (MZI) [62], Ring Resonators (RR) [63], grating couplers [64], among others. In many occasions, an optical spectrum is acquired, since induced changes in the on-chip optical signals are reflected in the power spectral density [65]. In photonics integrated circuits, there are two building blocks employed as spectrometers: the Arrayed Waveguide Gratings (AWG) [66] and Echelle Diffraction Gratings (EDG) [67]. The EDG is mainly employed for compact device designs, while AWG is used in a large variety of applications due to its reconfiguration capability [68]. AWG devices have been mainly employed for optical telecom applications, operating at 1530–1565 nm wavelength range. However, since sensing applications cover a much wider spectrum range, AWG spectrometers working from the visible (620 nm) [69] up to long near-infrared wavelengths (5 μm) [70] have been demonstrated. Optical spectrometers sensors are mainly applicated for Raman [71] or absorption spectrum analysis [69, 72, 73]. In the case of absorption spectroscopy applications, the sensor for glucose analysis presented in [73] employs

a broadband source and a tunable filter to perform the spectroscopic study. On the contrary, devices presented in [69] and [72] take advantage of the intrinsic demultiplexing feature of AWG to avoid the use of bulky instrumentation to realize the analysis. As can be seen from these examples, in order to perform the spectroscopic analysis of the sample, an integrated spectrometer is built together with the sensing architecture.

The Integrated Optical Spectroscopic Sensor (IOSS) presented in this thesis combines the sensing and spectral analysis in a single device. The IOSS is based on the Interleave-Chirp AWG (IC-AWG), reported by C. Doerr in 1998, which is applied for coherent optical communications [74–76]. The proposed device possess two clear advantages when compared with the architectures above discussed. Firstly, IOSS allows reference and sensing simultaneous measurements, hence, the results are not affected by the surrounding conditions.Relative measurements between the reference and sensing channels are always taken as the final result, as done in [73]. And secondly, sensing and spectral measurements are performed in a single device so the complexity of the PIC is reduced.

1.4 Objectives

The general objective of this Ph.D. is to bring the features of conventional bulk spectrometers into a compact PIC spectrometer sensor, of application on the telecom and visible wavelength range based on a new Silicon Nitride technology. To accomplish this goal, the following sub-objectives are considered:

1. The support in the development of a new Si_3N_4 platform with the characterization of the technology.

2. The development of the analytical model describing the operation of an integrated spectroscopic sensor (IOSS), as well as its design procedure.

3. The design, fabrication and characterization of the IOSS proof of concept as a validation of the model and verification of the sensing capabilities of the device.

1.5 Thesis outline

The thesis is structured in the following chapters, in line with the defined objectives:

- Chapter 2: the description of the Silicon Nitride technology employed in this thesis is detailed. The characterization of the platform is performed employing different test structures. The implementation of fabrication variations and extra step processes implementation is also analysed to find the best fabrication procedure.

- Chapter 3: the concept of the IOSS is presented, followed by its mathematical modelling based on Fourier optics. The design procedure is derived from the model. Finally, two reference designs working in the visible and mid infrared wavelength ranges are reported.
- Chapter 4: the design and characterization of the IOSS proof of concept is reported. Several AWG and IOSS configurations are fabricated to analyse in deep the response of the device. A second design and fabrication iteration is performed to improve the features of the device.
- Chapter 5: the thesis conclusions and open research lines are presented.

Chapter 2
Silicon Nitride Photonic Integration Platform

The general objective of this chapter is to present the Silicon Nitride platform on which all the devices of this thesis have been manufactured. The methodology and results of the optical characterization of the technology are reported. The chapter is structured as follows: the motivation and main characteristics of our Si_3N_4 platform are summarized in Section 2.1, while the fabrication process is explained in detail in Section 2.2. The optical characterization of the technology is described along Sections 2.4, 2.5 and 2.6, where the setup and test structures employed are described, as well as the physical parameters established as figures of merit. The impact on the optical properties depending on fabrication processes have been also estudied in Section 2.7. Finally, the chapter conclusions are presented in Section 2.8.

2.1 Silicon nitride platform 300 nm film height.

The Si_3N_4 platforms state of the art compiled in Table 1.1 is summarized in Table 2.1 in terms of the confinement and wavelength range. Each of the platforms will be chosen depending on its suitability for the desired application. Low confinement waveguides are usually employed in linear applications, such as optical delay lines, whereas high confinement waveguides aim at having the lowest non-linear effects threshold as possible. The aim of this project was to develop a versatile platform operating in a wide range of the spectrum, and therefore being able of covering diverse photonic integrated applications in the field of bio-photonics, tele/datacom and sensors.

High confinement waveguides operating in the NIR and NIR+ range, are mainly employed for non-linear optical signal processing, as for example frequency comb and super-continuum generation [38,77–79]. Nevertheless, there are also non-linear

Confinement	h (nm)	Range	Wavelength (nm)	Loss (dB/cm)
Low	80–100	NIR	1550	0.02–0.09
Moderate	150–400	NIR	1270–1600	0.11–1.45
High	400–1200	NIR	1550	0.04–1.37
High	950–2500	NIR+	2600–3700	0.16–2.10
Moderate	100–220	VIS+	532–900	0.51–2.25

Table 2.1: Summarized comparison of silicon nitride strip waveguide platforms.

applications reported in the VIS+ range, employing moderate confinement waveguides [80]). From a fabrication perspective, core heights of this last configuration (100 - 400 nm) can be obtained in a single deposition step, which reduces the risk of nitride cracking due to stress issues (see for instance [40]).

When the application requires low propagation losses, low or high confinement platforms are more suitable. As it was mentioned in the previous section, the propagation loss is highly related with interaction of the propagating mode with sidewall roughness [29]. For both low and high confinement waveguides, the mode interaction with the sidewall is minimal, so propagation losses will in turn be low. In terms of polarization, low confinement platforms are strongly polarization dependent (i.e., only one polarization is guided as for instance in [34]), whereas high confinement ones suffer of multi-modal effects-lateral and vertical—(cf. [81]).

As can be seen, low and hight confinement platforms are more appropriate for applications working in a specific wavelength range. By contrast, moderate confinement platforms can host applications in a wider spectral range, for which they are considered versatile platforms, at the expense of reduced performance. Very recently, the key actors providing silicon nitride foundry services on open-access scheme have reported their technologies on a review paper [82]. Considering all the above and having in mind our objective, we developed a Si_3N_4 on SiO_2 platform with Si_3N_4 guiding film height of 300 nm covering a range of the spectrum from 400 to 3700 nm. The fabrication process and characterization of the technology around 1550 nm is reported in following sections.

2.2 Fabrication Process.

The fabrication process starts by growing a 2.5 μm thick SiO_2 buffer by thermal oxidation of a Si wafer of 100 mm (4 inch). Following, a 300 nm layer of Si_3N_4 is deposited by low-pressure chemical vapour deposition (LPCVD). In the next step, the waveguide cross-section are patterned by photo-lithography employing an i-line stepper, which minimum feature size is 500 nm. Afterwards, the definition of the core cross-section is accomplish by reactive ion etching (RIE) of the silicon nitride film. Two different waveguide cross-sections can be implemented by controlling the etching depth. If the silicon nitride layer is completely etched, a strip waveguide structure (DEWVG in Figure 2.1) is formed. If the etching is done partially, a rib waveguide structure (SHWVG, Figure 2.1) is obtained (300 nm/150 nm). Lastly,

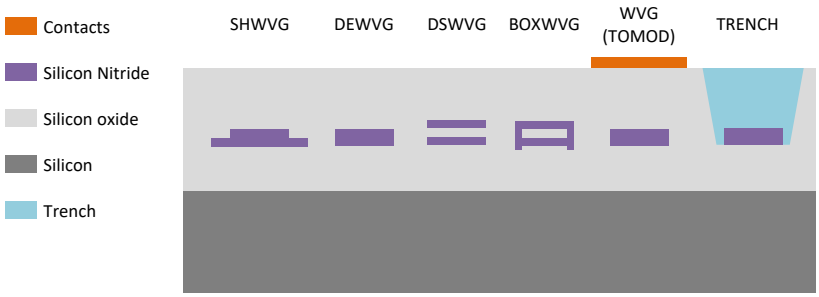

Figure 2.1: Silicon Nitride photonics platform cross-sections.

a SiO_2 cladding of 2 μm thickness is deposited by means of Plasma Enhanced CVD (PECVD), whereby the guides are fully defined. After the waveguide fabrication steps, two additional processes allow to fabricate thermo-optic tuners, and to create air wells by selectively etching away the cladding oxide. Metal heaters (TOMOD, Figure 2.1) are defined by lift-off process. Firstly, a sacrificial layer is deposited and an inverse pattern is created. Then, the metals are deposited, by sequential evaporation, obtaining a 10 nm thick Chromium layer under 90 nm thick Gold layer. Finally, the sacrificial layer together with the surplus material is removed. The air wells (TRENCH, Figure 2.1) generate areas where the waveguide core is in direct contact with the surrounding media. TRENCH structures are opened into the SiO_2 cladding layer down to the bottom of the silicon nitride guiding layer. They are firstly defined via photo-lithography, and then created by RIE in two etching steps, to reduce the waveguide top damaging risk. These structures are mainly employed for (bio)chemical sensors applications [83].

2.3 Si_3N_4 waveguide simulations.

The guiding properties of the strip (DEWVG) and rib (SHWVG) waveguides were simulating employing a mode solver software (Synopsys Inc., OptoDesigner Software, [84]). We firstly determined the effective refractive index for the first order mode and the two polarizations around 1550 nm wavelength. This was done for both waveguides cross-sections with film height and waveguide width of 300 nm and 1000 nm respectively. The results are shown in Figure 2.2-a. For the case of the SHWVG cross-section, the TM mode does not propagates along the waveguide.

The group refractive index, which is derived from:

$$n_g = n_{eff}(\lambda_0) - \lambda_0 \frac{dn_{eff}(\lambda)}{d\lambda}\Big|_{\lambda=\lambda_0} , \tag{2.1}$$

where λ is the wavelength of the propagating light, was also obtained 2.2-(b). The propagation mode profiles for TE and TM polarizations at 1550 nm wavelength

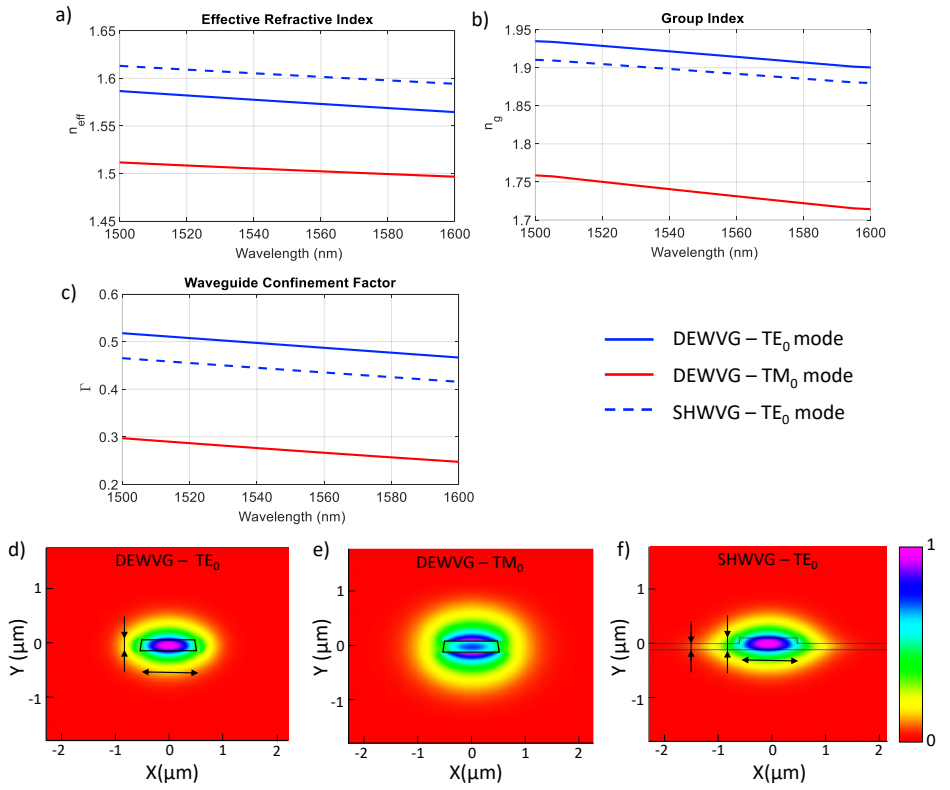

Figure 2.2: Effective refractive index (a), group index (b) and confinement factor (c) for TE and TM polarizations for strip (DEWVG) and rib (SHWVG) waveguides. Figures (d), (e) and (f) represent the waveguide cross-section and the mode profile at $\lambda = 1550$ nm for fundamental TE and TM modes for both waveguides cross-sections. TM_0 mode in SHWVG waveguides is not propagated at this wavelength range.

are represented in Figures 2.2-c and 2.2-d) for both DEWVG and SHWVG cross-sections.

2.4 Measurement setup and test structures.

In order to asses on the optical performance of the platform, several type of test structures (TS) were designed and characterized using an Optical Frequency Domain Reflectometry (OFDR) setup [85–88]. This setup is composed of two imbalanced MZIs in standard single-mode fiber, connected in parallel and fed by a scanning Tunable Laser (TL), Figure 2.3. The device under test (DUT), in our case the Si_3N_4 chip, is placed in the upper MZI (DUT-MZI). In/out coupling can be

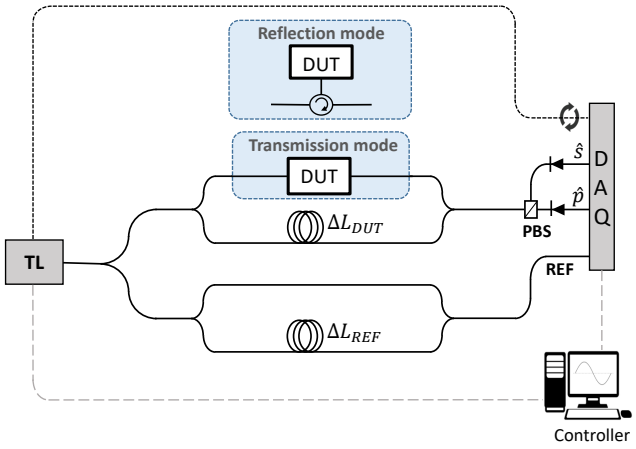

Figure 2.3: Optical frequency domain reflectometry setup. Abbreviations: Device under test (DUT), Reference (REF), polarization beam splitter (PBS).

done either through lensed fibers or microscope objectives. A Polarization Beam Splitter (PBS) is connected to the output fiber and before the photodetectors to acquire both interferograms. Finally, the signals are collected by a Digital Acquisition (DAQ) card. This disposition prevents the destructive interfering effects due to polarization missalignment between both MZI arms, as described in [86,87]. The lower MZI is employed as triggering (TRIG-MZI), since the DUT-MZI response is resampled (offline) by points provided by TRIG-MZI interferogram. This ensures that the DUT-MZI response is self-referenced against possible nonlinearities of the continuous TL scan. As described in [85–87], the time response of the DUT (amplitude and phase) can be isolated by applying the Inverse Fast Fourier Transform (IFFT) to the DUT-MZI interferogram. The TS employed were spiral waveguides, Mach-Zenhders interferometers and single bus-coupled ring resonators. The spiral waveguides were employed, alongside the setup in reflection mode (an additional circulator is required, Figure 2.3) to obtain the propagation loss. In turn, the ring resonators are useful to isolate pulse recirculation in the interferograms, and derive the group index, (n_g), and Group Velocity Dispersion (GVD) from the progressively broadened pulses [89].

2.5 Propagation Loss.

We employed two different TS to characterise propagation losses: i) spirals waveguides, through OFDR backscattering measurements and, ii) MZIs, via its transmission spectrum [90]. Figure 2.4-a shows the spiral waveguide structure, composed by two smaller spirals of 1 and 2 cm long respectively and 1 μm width (measured at the top surface of core waveguide). This width ensures that the

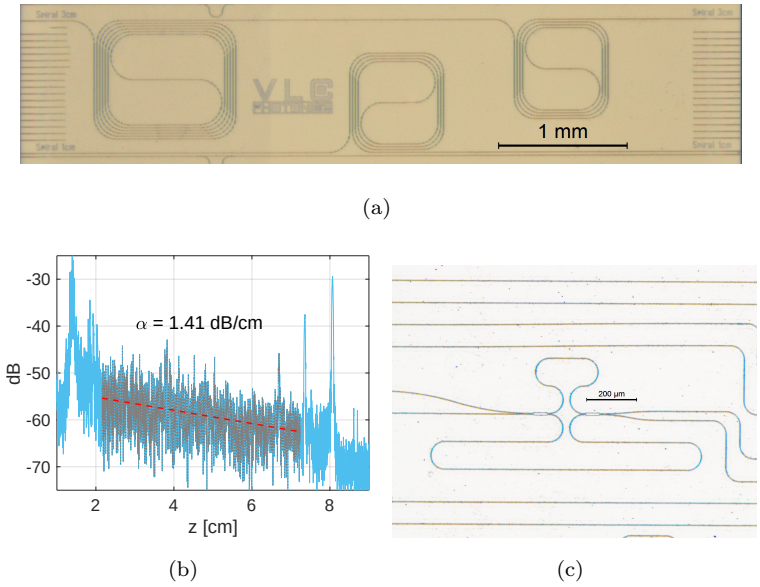

Figure 2.4: Test structures devised for the characterization of the propagation loss. (**a**) Spiral waveguides devices. (**b**) optical frequency domain reflectometry trace from spiral waveguide. Light blue trace represents the direct measurement, while grey shaded area corresponds to the range selected for a linear fit, which is shown in the figure as dashed red line. (**c**) Mach-Zehnder Interferometer device.

fundamental mode is the only mode supported and it is fixed in all the designed devices. The bend radius was settled to 150 μm to minimize bend losses, which were negligible according to the full-vectorial mode solver simulations. An OFDR acquired measurement in reflection mode is shown in Figure 2.4-b. the highest peaks appearing on the outermost parts of the trace represents the in (left) and out (right) coupling of light. Propagation loss was calculated from the linear fitting of the center part of the trace (black color). These measurements were performed without polarization controller, therefore the propagation loss obtained should be taken as an illustrative value, since it is the average of both polarization over the wavelength range swept. Several samples were characterised showing good repeatability in the results.

We employed the MZI test structure to cross-check the information obtained from the spirals. A microscope picture of the designed MZI is shown in Figure 2.4-c. Bend radius was settled to 50 μm in this occasion to reduce the device footprint. The path difference was designed to be only in the straight sections. The couplers employed in the MZI layout are 2 $\times$ 2 50:50 MMI couplers. The four transmission spectra (input-output combinations) were acquire using a broadband Amplified Spontaneous Emission (ASE) source and an Optical Spectrum Analyser (OSA) as

detector, as described in [90].

Propagation loss derived from both devices was in the range of 1.2–1.6 dB/cm. As it will be discussed in Section 2.7, further fabrication steps can be applied to improve the guiding properties, as for example Si_3N_4 thermal annealing, which reduces de propagation loss in the optical telecom C-band [29]. Taking into account that no such processes have been applied in this fabrication run, the propagation loss in in agreement with similar waveguide cross-sections, cf. [32, 47] and Table 1.1.

2.6 Group Index and Dispersion.

A Ring Resonator (RR) was the test structure selected to obtain group index and dispersion parameters. Figure 2.5-a shows a picture of the fabricated device. It is a single bus RR coupled through a 2×2 50:50 MMI coupler to a straight waveguide. Bend radius was settled to 150 μm, since the effective index versus wavelength relation of these bends is similar to a straight waveguide (according to full-vectorial mode solve simulations), at the same time as keeping the device foot-print as compact as possible. The total length of the ring perimeter was 6.63 mm.

The OFDR measurements were performed with the TL scanning at a speed of 40 nm/s along 80 nm (span), centered at 1550nm. Following the procedure explained in Section 2.4, the time response of the device ($|h(t)|^2 = |h_s|^2 + |h_p|^2$) was obtained, as shown in Figure 2.5-b. Each pair of peaks of the trace correspond to multiple recirculations of TE and TM propagating modes inside the RR. It can be seen how the peaks corresponding to TE and TM are separated in time, due to the difference between their effective refractive indices (and, consequently, group index difference). Group index values can be calculated knowing the time difference between consecutive peaks and the cycle length (perimeter) of the RR. The experiment reported group indices of 1.892 and 1.717 for TE and TM modes, respectively.

To cross-check these results, the group index was also inferred from MZI spectra transmission measurements for TE mode. Group index was in the range of 1.90–1.92, which is in agreement to that obtained through OFDR measurements. The TE and TM propagation delay difference leads to a value of, $|n_g^{TE} - n_g^{TM}| = 0.168$.

The broadening effect caused by the Group Velocity Dispersion (GVD) can be already noticed in 2.5-(b). This effect is more noticeable when each peak is isolated and responses from consecutive pulses are compared. Figure 2.5-c shows the first four contributions of TE mode. These responses are transformed into the frequency domain to calculate the group delay [86, 87]. A linear fitting between 1514 and 1594 is done to obtain the dispersion parameter D (ps/(nm·m)) of each contribution (Figure 2.5-d).

We expected the D values to be constant, however the results showed certain variability. This suggests that the measurement setup dispersion was embedded in the result. To decouple setup and device dispersion parameters, we compared

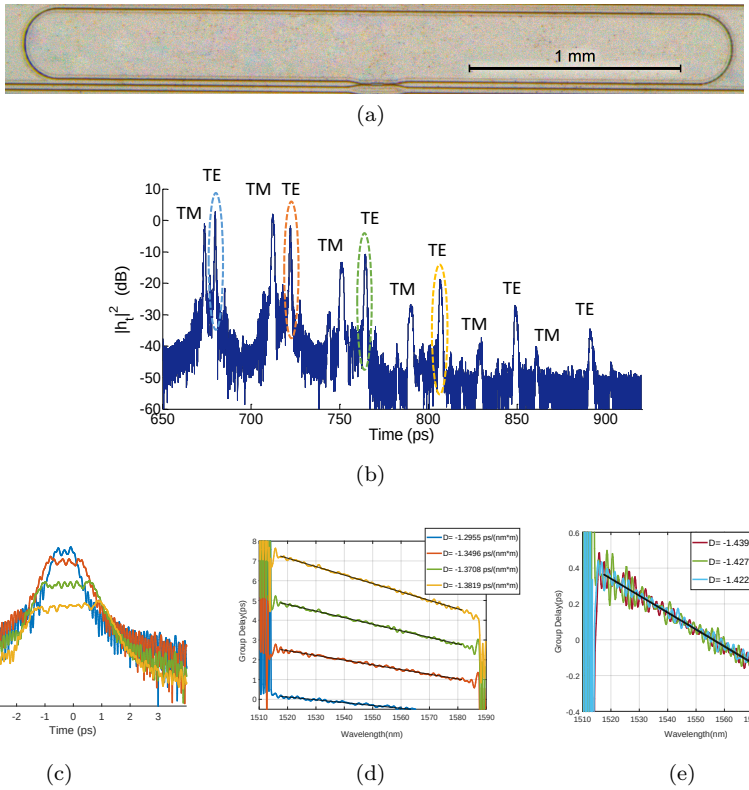

Figure 2.5: (**a**) Ring resonator test structure devised for the characterization of the group index (n_g) and the group velocity dispersion (GVD), (**b**) Optical Frequency Domain Reflectometry (OFDR) trace from the ring resonator, with TE and TM pulses labelled, (**c**) TE pulses sliced and collated, exhibiting broadening due to GVD, and (**d**,**e**) group delay and corresponding dispersion.

consecutive RR contributions per pairs to isolate a single round trip along the ring. This comparison is represented in Figure 2.5-e, where a linear fit was performed to obtain the dispersion over the wavelength range of interest. This results into an average dispersion of D = −1.43 ps/(nm·m) with a relative error of ±1.5%. From these values it is straightforward to obtain the dispersion offset from the set-up as $(D \cdot L)_{setup} = 0.0014467$ ps/nm.

2.7 Fabrication Process Steps Variations.

The propagation properties of the waveguides can be improved by applying extra steps to those already described in Section 2.2, during the fabrication process. In

#	BOX h0 (μm)	Si_3N_4 h1/h2 (μm)	Si_3N_4 OX	Cladd. RTA	α_{de} (dB/cm)	$n_{g,de}^{TE}$	GVD_{de}^{TE} (ps/nm·m)	α_{sh} (dB/cm)	$n_{g,sh}^{TE}$	GVD_{sh}^{TE} (ps/nm·m)
A1	2.0	284/155	no	no	2.36	1.89	-0.9	n.a.	n.a.	n.a.
A2	2.0	289/153	yes	no	1.47	1.87	-1.43	n.a.	n.a.	n.a.
B1	2.5	299/147	no	no	2.07	1.93	-0.87	n.a.	n.a.	n.a.
B2	2.5	300/143	yes	yes	1.79	1.89	-1.37	n.a.	n.a.	n.a.
C1	2.5	281/155	yes	yes	0.99	1.86	-1.32	1.77	1.96	-0.92
D1	2.5	299/157	yes	yes	2.27	1.76	-1.98	2.02	1.94	-1.14
D2	2.5	301/155	yes	no	1.66	1.71	-2.07	1.20	1.95	-1.11
D3	2.5	301/156	no	no	1.89	1.76	-2.11	1.35	1.95	-0.95
D4	2.5	300/155	no	yes	1.76	1.78	-1.98	1.97	1.95	-0.88

Table 2.2: Design of experiments and results for deeply and shallowly etched waveguides. (n.a. data not available)

other to find the best fabrication recipe, different manufacturing processes steps were investigated. This was done through several fabrications runs in which the processes were progressively modified to finally compare the results of each one of them. The processes/modifications that were investigated were three: i) variation of buried oxide (BOX) layer height, ii) thermal oxidation of the Si_3N_4 layer and iii) Rapid Thermal Annealing (RTA) of the SiO_2 cladding. The thermal oxidation of the Si_3N_4 layer was performed after etching and prior cladding deposition, with the aim of reducing the sidewall roughness. It should be noted that the Si_3N_4 cross-section is slightly reduced after oxidation, since oxynitride is grown at the expense of Si_3N_4. On the other hand, RTA is a densification process, which generates a increase of the refractive index, as well as a reduction of the cladding height.

All the information about the different wafers fabricated and the processes applied to each one of them, is collected in Table 2.2. The experiments were performed in four different fabrication runs (A, B, C and D). These have been developed at different times, so all the samples among them can be considered fully independent along all the process steps, described in the previous section, from deposition, through patterning, dicing and test.

The first column of Table 2.2 details the fabrication run (letter) and the wafer (number) analysed. Second and third columns specify the substrate ($h0$) and core waveguide heights respectively. $h1$ and $h2$ refer to the DEWVG and SHWVG core cross-section heights, respectively. Four and fifth columns specify either if the extra processes described above (oxidation, OX, and RTA) have been applied or not. Sixth to ninth columns report the average values of propagation loss, group index and GVD for DEWVG waveguides obtained from TS measurements. Same parameters are depicted for SHWVG waveguides in the last three columns. Run A wafers present lower BOX height ($h0 = 2.0\mu$m) than the rest of the wafers ($h0 = 2.5\mu$m). In turn, runs A and C have slightly shorter Si_3N_4 core height for both DEWVG and SHWVG cross-sections.

2.7.1 Propagation loss discussion.

Propagation loss values detailed in Table 2.2 are graphically represented in Figure 2.6 for ease of comparison. In case of runs A and B, only strip (DEWVG) wa-

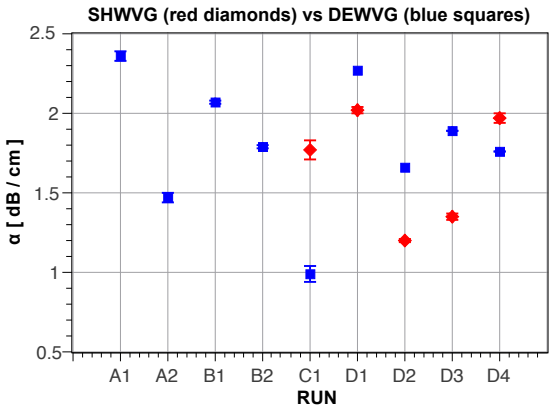

Figure 2.6: Values of propagation loss coefficient for DEWVG and SHWVG waveguides, for the different samples of Table 2.2.

veguides were studied. The discussion for each waveguide cross-section (DEWVG and SHWVG) will de done separately. Regarding DEWVG waveguides, wafers A1, B1 and D3 can be taken as reference samples, since no additional processes (Si_3N_4 OX or Cladd. RTA) have been applied to them. Among these three reference samples, A1 is the one presenting the largest α_{de}, which can be attributed to its shorter BOX height ($h0$).

By comparing A1-A2, B1-B2 and D3-D2 wafers, it is clear that the Si_3N_4 oxidation results into a reduction of the propagation loss, which is in good agreement with previous works published about this technology [29]. The influence of oxidation in the propagation loss is comparatively presented in Fig. 2.7. Both show the OFDR measurement of spiral waveguide test structures for a wafer not subject to oxidation (c) and other where oxidation was applied after etching the waveguides (d). Two effects can be clearly appreciated. The trace in (c) shows intensity peaks along the spiral (i.e., most relevant between z = 0.5 and z = 2.5 cm). The examination with a scanning electron microscope (SEM), revealed the waveguides had severe damage on the top edges and sidewalls 2.7-(a,b), likely due to high energy centers caused by resist concentration points during etching. These peaks are removed with the oxidation, confirmed by SEM imaging of the sample, for which the OFDR measurement is shown in Fig. 2.7-(d). Furthermore, the propagation loss difference between (b) and (c), obtained by comparing the fitted lines, is approximately 1 dB lower for the oxidized wafer.

Runs B and D show similar results. However, since the fabrication process steps were progressively applied in run D wafers, clearer conclusions can be drawn from them. The results from direct RTA process application can be observed by D3 and D4 wafers comparison. When only the RTA process is applied, α_{de} slightly decreases. However, when RTA is applied after oxidation (OX) process (D2-D1 comparison), the propagation loss is worsened, which may be due to the residual hydrogen that is diffused from the cladding PECVD SiO_2 to the Si_3N_4 layer.

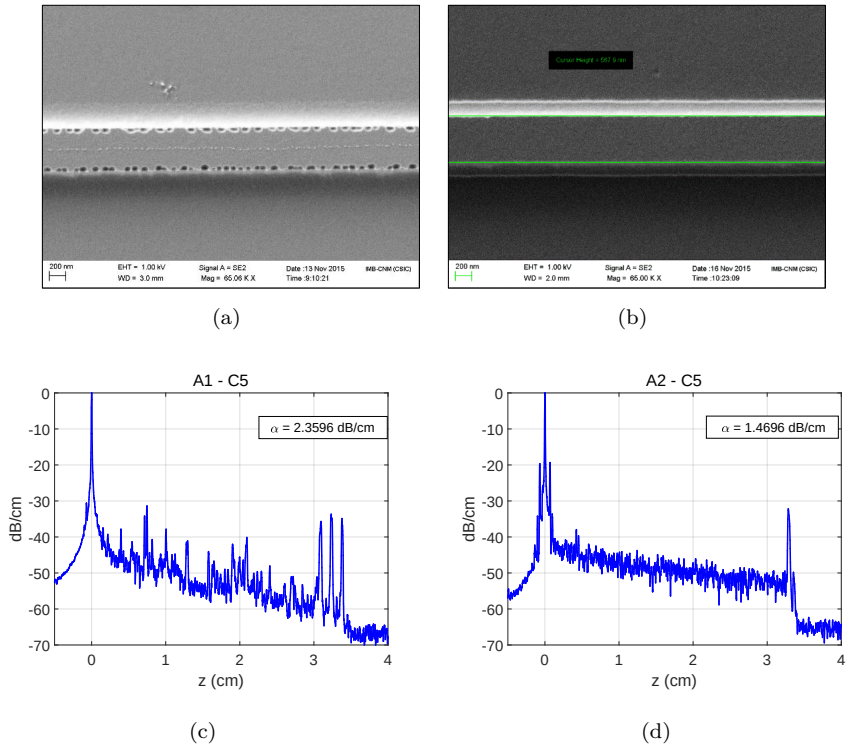

Figure 2.7: SEM pictures of a waveguide section without (**a**) and with (**b**) oxidation of the Si_3N_4 layer after etching; OFDR measurement for spiral waveguides no subject (**c**) and subject (**d**) to oxidation process.

The lowest propagation loss for strip waveguides is achieved by wafer C1. This sample can be contrast with B2 and D1 runs, since all of them have gone through the same fabrications processes. They only differ in the Si_3N_4 guiding layer height ($h1$), being shorter in the case of C1 ($h1 = 281$nm vs nominal $h1 = 300$nm). In the case of C1, the mode is less confined (more light is guided through SiO_2) and, therefore, the interaction of light with sidewall roughness is less. Hence, propagation losses are decreased in this case, as it was explained in Section 1.2 for low confinement waveguides. Regarding shallowly etched (SHWVG) waveguides, we only own information for C and D runs. D wafers comparison, taking as reference D3, lead to same conclusions than for DEWVG: oxidation process improves the propagation loss, whereas RTA yields increased propagation loss when applied after oxidation. C1 shows lower propagation losses than D1, but this can be again attributed to the reduced Si_3N_4 height.

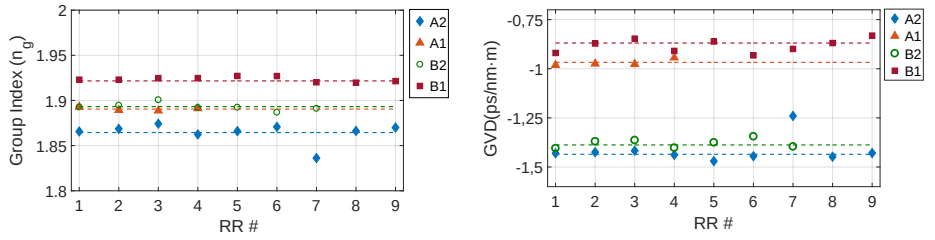

(a) (b)

Figure 2.8: Impact on process steps on the linear propagation characteristics. TE polarization mode group index (**a**) and GVD (**b**) for the different processing steps implemented.

2.7.2 Propagation constant and derivatives discussion

In this case, the comparison of the fabrication processes was performed separately for runs A-B and D since they were fabricated in different periods of time and only DEWVG waveguides were analyzed for A and B runs. Beside, runs A and B were subjected to a more detailed study, characterising RR test structures placed in the different cells in which a wafer is sliced (see Figure 1.1). The impact on the group index and dispersion depending on the fabrication process is shown in Figures 2.8, for A and B runs, and 2.9, for D runs. In turn, the results for all the runs are provided in Table 2.2.

Figure 2.8 shows TE polarization mode group index and dispersion results from several RR evaluated for each A and B fabrication runs. When comparing wafers A1 (reference) and A2 (wafer with OX process applied), represented by orange triangles and blue diamonds respectively, a decrease of the group index can be observed. This can be attributed to a reduction of both waveguide dimensions and index contrast reduction, since the oxidation process generates an oxyinitride interlayer between Si_3N_4 guiding layer and SiO_2 cladding. This in turn results in a less confined mode and therefore reduced effective index, which is one of the two terms (additive) in the group index expression (eq. 2.1).

The same applies to rounds B1 and B2 (red squares and green circles, respectively). However B2 has also gone through RTA process and the difference of group index between both B runs ($n_g^{B1} - n_g^{B2} = 0.04$) is higher than for A runs ($n_g^{A1} - n_g^{A2} = 0.02$). It is difficult to determine if this difference is due to RTA process, since it can be also attributed to the variations in the heights of substrate (BOX) and Si_3N_4 layers between A and B runs. Comparison between fabrication runs D will bring more information about this process.

The influence on the waveguide dispersion, measured from RR devices with the OFDR technique as previously shown in Section 2.6, is presented in Figure 2.8-b. The impact of Si_3N_4 oxidation can be clearly observed, by comparing the traces corresponding to A1 and A2 (orange triangles and blue diamons, respectively).

A change in the dimensions of the waveguide can be directly correlated with a change in the waveguide dispersion, as seen in the graph. Similar conclusion can be applied for B runs.

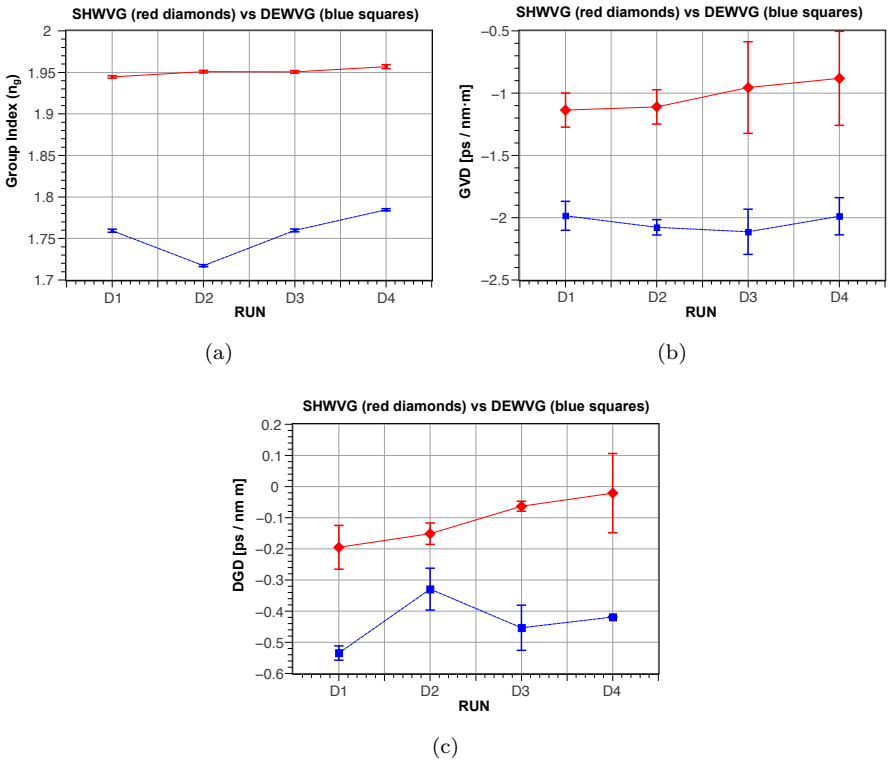

Figure 2.9: (a) Group index, (b) Group Velocity Dispersion and (c) Differential Group Delay, $DGD = GVD^{TE} - GVD^{TM}$, measured for shallowed (red diamond) and deeply (blue square) etched waveguides for TE polarization.

From the results of A and B runs, we concluded that the correct procedure was to compare dies and structures that were placed at the same spot of the wafer. During the fabrication of the wafer, the growth of the different material layers is not completely homogeneus (±10 nm, in height from external to central regions), and hence, the propagation characteristics may vary (slightly) between dies in the same wafer. Therefore, comparison between D runs was performed characterizing the central die of each wafer.

Group index results from run D are shown in Figure 2.9-a, for both strip (DEWVG) and rib (SHWVG) waveguides. From D3 and D2 comparison, one can note how oxidation of the nitride layer results in a reduction of the group index for the DEWVG waveguide, which is coherent with the results obtained for A and B runs. Contrasting D3 and D4 runs, the RTA of the cladding results into an

increase of the group index. On the contrary, both oxidation and RTA have slight impact on the SHWVG waveguide group index.

The corresponding GVD values are represented in Figure 2.9-b with error intervals. The error bars of the different processed wafers are clearly overlapped, which prevent as to draw clear conclusions, since this uncertainty might be also dragged to the post-processing. Nevertheless, the average results obtained for n_g and GVD are in agreement with the simulated values (Section 2.3).

For these runs, information from both TE and TM polarization modes was obtained. Figure 2.9-c shows the propagation delay difference between both polarization, which is related to the birefringence of the waveguides. Figure 2.9-d, represents the Differential Group Delay (DGD) between TE and TM modes.

2.8 Conclusions

In this chapter, a review of the present state of the art of silicon nitride photonic integration platforms has been presented, as well as the main features of each one of them. Our progress in developing a moderate confinement platform in the optical telecom C-band has been also detailed. The manufacturing process of the platform has been reported, which includes fewer manufacturing steps than the rest of the nitride platforms. This offers a more accesible platform for everyone, having optimal parameters for the propagation of light. Fabrication design of experiments, with subsequent full-field measurements of test spiral waveguide and ring resonator test structures, allowed to correlate the process step variations to different optical waveguide features, such as the propagation loss and group velocity dispersion, which are of high interest in current developments of linear and non-linear integrated photonics applications. The review has been complemented with modeling and experimental results for a versatile 300 m Si_3N_4 guiding film height platform, with canonical waveguide width of 1μm. The choice of advanced full-field characterization techniques and suitable test structures, allowed to obtain the propagation loss for strip waveguides (DEWVG) between 1.4 - 1.6 dB/cm, group index around 1.85, and dispersion between -1.4 ps/nm m and -2.07 ps/nm m, while for rib waveguides (SHWVG) the propagation losses are 1.2 dB/cm, 1.95 for group index and -1.11 ps/nm m for dispersion.

The results obtained through this chapter have been reported in the following publications:

- P. Muñoz, G. Micó, L. A. Bru, D. Pastor, D. Pérez, J. D. Doménech, J. Fernández, R. Baños, B. Gargallo, R. Alemany, A. M. Sánchez, J. M. Cirera, R. Mas and C. Domínguez, "Silicon Nitride Photonc Integration Platforms for Visible, Near-Infrared and Mid-Infrared Applications", *Sensors*, vol. 17, no. 2088, 2017.

- G. Micó, L. A. Bru, D. Pastor, J. D. Doménech, A. M. Sánchez, C. Domínguez and P. Muñoz,"Impact of manufacturing processes on the optical amplitude, phase and polarization properties of silicon nitride waveguides" *20th Euro-*

pean Conference on Integrated Optics (ECIO), Valencia, Spain, 30th May - 1st June 2018.

- G. Micó, L. A. Bru, D. Pastor, D. Pérez, J. D. Doménech, J. Fernández, R. Baños, B. Gargallo, R. Alemany, A. M. Sánchez, J. M. Cirera, R. Mas, C. Domínguez P. Muñoz, "Silicon nitride photonic integration platform for visible, near-infrared and mid-infrared applications" *XIV European Conference on Optical Chemical Sensors and Biosensors (Europtrode XIV)*, Naples, Italy, 25th - 28th March, 2018.

- G. Micó, L. A. Bru, D. Pastor, J. D. Doménech, J. Fernández, A. M. Sánchez, J. M. Cirera, C. Domínguez and P. Muñoz, "Silicon nitride photonics: from visible to mid-infrared wavelengths" *SPIE Photonics West 2018 - Silicon Photonics XIII*, San Francisco, California, United States, February 2018.

- G. Micó, L. A. Bru, D. Pastor, D. Pérez, J. D. Doménech, A. M. Sánchez, J. M. Cirera, J. Sánchez, C. Domínguez P. Muñoz,"C-band linear propagation characteristics for a 300 nm film height Silicon Nitride photonics platform" *19th European Conference on Integrated Optics (ECIO)*, Eindhoven, The Netherlands, 3rd - 5th April 2017.

Chapter 3
Integrated Optical Spectroscopic Sensor

In this chapter, the concept and description of a new spectroscopic sensor architecture is reported. The device in named Integrated Optical Spectroscopic Sensor (IOSS) and is based on a modified configuration of an Arrayed Waveguide Grating (AWG). The IOSS combines evanescent field sensing and spectrometric analysis in a single device, and can be employed for absorption spectroscopy applications. The chapter is structured as follows: the concept and main characteristics of our device are explained in Section 3.1, while its operation and the mathematical formulation is delailed in Section 3.2. The design procedure followed to generate the layout is described is Section 3.3. For completeness, in Section 3.4 two reference designs are shown as example of design process in two wavelength ranges of application: visible range (Section 3.4.1) and infrared range (Section3.4.2). To finish, the conclusions of the chapter are stated in Section 4.3.

3.1 IOSS device concept

An integrated AWG consist of two slab couplers acting as Free Propagation Regions (FPR) interconnected by a plurality of waveguides, commonly called arrayed waveguides, AW (Figure 3.1-a). There is a constant incremental length between consecutive AW, ΔL, which induces a phase shift depending on the light wavelength propagated. Light is coupled through the central input waveguide and propagated afterwards along the first FPR. The diffracted light is then coupled into the multiple arrayed waveguides. When light reaches the second FPR, the contributions of all the AW are added together. At this point, light propagating at different wavelengths focuses at distinct positions (focal points) along plane X_3 (Figure 3.1-a), and each of these optical signals is known as a AWG channel. The process of dividing the input beam into its multiple wavelengths is called demulti-

plexation, which in the case of an AWG is achieved due to the accumulated phase difference generated in the arrayed waveguides, in combination with the second FPR.

The Integrated Optical Sensing Spectrometer (IOSS) is based on a Interleaved Detuned-AWG (ID-AWG), as explained below. IOSS operation is represented schematically in Figure 3.1-b. As can be seen, the IOSS is composed of the same elements as a conventional AWG: input/output waveguides, two slab couplers employed as Free Propagation Regions (FPRs), and an array of optical waveguides connecting both FPRs. However, IOSS arrayed waveguides are divided into M subsets, known as sub-arrays. Each sub-array has a defined incremental length, ΔL, between consecutive waveguides. Thus, the original Free Spectral Region (FSR) of the device is reduced by a factor M, as will be explained in detail in the following section. In other words, the creation of sub-arrays will generate M number of replicates of the AWG channels. In the example presented in Figure 3.1-b, M was set to 2 to simplify the explanation. Sub-arrays are represented by dashed and solid lines, and they are interleaved as in [74–76]. The channels generated by the sub-arrays are set apart (detuned) by design along plane X_3, which is controlled by the length increment between consecutive waveguides, ΔL [91]. Hence, the output plane is divided into two halves, each one independently collecting the optical signals coming from each sub-array.

One of the sub-arrays is employed as reference of the input signal (reference sub-array), while the other is employed for sensing (sensing sub-array). Arms of the sensing sub-array are provided with sensing windows (Figure 3.1-c) defined by selective area etching, as explained in Section 2.2. In these windows, the sample under study interacts with the evanescent optical field in the waveguides. Hence, when the sample is placed on top of the device, only the sensing channels are altered, while reference channels remain unperturbed. The relative change between reference and sensing signals can be correlated with the presence and concentration of the sample under study through two different interrogation methods: i) Intensity interrogation, by tracking changes in the signal due to sample absorption, and ii) Wavelength/frequency interrogation, by monitoring the wavelength/frequency shift of the corresponding channels due to phase changes induced by the sample. This wavelength/frequency shift is translated into a spatial displacement of the channels in plane X_3.

Depending on the transduction method employed, the configuration of the IOSS sensing sub-array will change. In case of intensity interrogation, all the sensing windows are designed to have exactly the same length. Thus, the attenuation due to sample absorption will be similar in all the sensing waveguides. Moreover, since all windows have the same length, there is no phase change induced by the sample. For wavelength/frequency interrogation, the length of the sensing windows is set to have a constant incremental length between consecutive sensing waveguides (Figure 3.1-c) to encourage the phase shift due to light-sample interaction. These concepts are further explained in next section.

Since sample information is contained in each of the sensing channels, the response of the sample is recorded at different wavelengths (spectroscopic analysis).

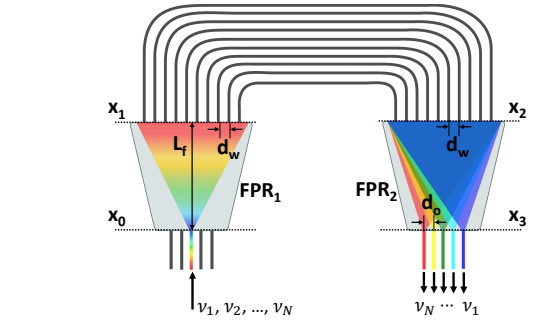

(a)

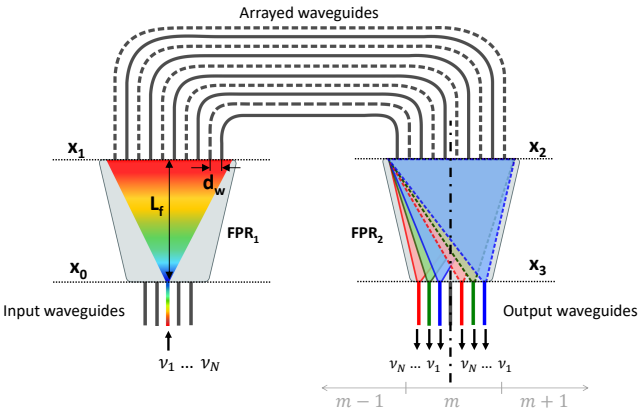

(b)

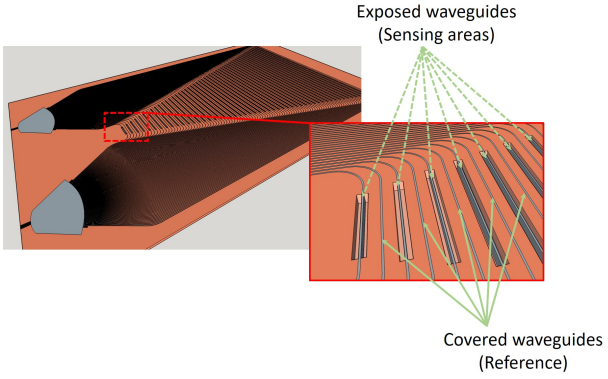

(c)

Figure 3.1: (**a**) Arrayed Waveguide Grating (AWG) operation scheme. (**b**) Integrated optics sensing spectrometer (IOSS) operation scheme. (**c**) IOSS layout for wavelength/frequency interrogation. Windows are opened (exposed waveguides) in one of the sub-arrays to interact with the sample (sensing sub-array), while the other sub-array remains covered (reference sub-array).

Hence, both reference and sample spectra can be acquired in a single measurement.

3.2 Device operation description.

The idea and description of the operation of an AWG was presented for first time in 1996 [91]. Since then, many analytical models have been proposed to simulate such devices [92]. The formulation described in this section follows the model and nomenclature employed in [68, 76].

At first stage, only one input waveguide is considered for simplicity. The chosen input waveguide is placed at the centre of plane X_0 (Figure 3.1-b), connected at the entrance of the first Free Propagation Region, FPR_1. The field at this input waveguide can be defined by a power normalized Gaussian function described by [68]:

$$f_0(x_0) = b_i(x_0) = \sqrt[4]{\frac{2}{\pi w_i^2}} e^{-\frac{x_0}{w_i}^2}, \tag{3.1}$$

where x_0 is the spatial coordinate at the input plane and w_i represents the mode field radius of light at the input waveguide. When light reaches the FPR_1, it is diffracted. The light power distribution at the output plane of FPR_1, X_1, can be obtained from the Fourier transform of the input light field, employing the paraxial approximation [93]:

$$B_i(x_1) = \frac{1}{\alpha}\mathcal{F}\{b_i(x_0)\}\Big|_{u=\frac{x_1}{\alpha}} = \sqrt[4]{\frac{2\pi w_i^2}{\alpha^2}} e^{-\left(\pi w_i \left(\frac{x_1}{\alpha}\right)\right)^2}. \tag{3.2}$$

In this equation, x_1 is the spatial coordinate at the FPR_1 output plane (Figure 3.1-a), u is the spatial frequency Fourier coordinate and α is the equivalent to the wavelength focal length product in Fourier optics propagation [68] defined as:

$$\alpha = \frac{cL_f}{n_s \nu}, \tag{3.3}$$

being c the speed of light in vacuum, L_f the focal length of the FPRs, n_s the effective refractive index of the slab coupler propagating mode and ν the frequency of light.

The mathematical description of an ID-AWG differs from the one of a conventional AWG when the terms of the multiple sub-arrays need to be introduced, which appear when light reaches the AWs. Each sub-array is characterized by a different incremental length, ΔL_k, being k an integer number defining each sub-array ($k = [0, M-1]$). Thus, the field at this plane is calculated as:

$$f_1(x_1) = \sqrt[4]{2\pi w_g^2} \sum_{k=0}^{M-1} \left[\prod\left(\frac{x_1}{N d_w}\right) B_i(x_1) \sum_{r=-\infty}^{+\infty} \delta(x_1 - M r d_w - k d_w) \right] * b_g(x_1), \tag{3.4}$$

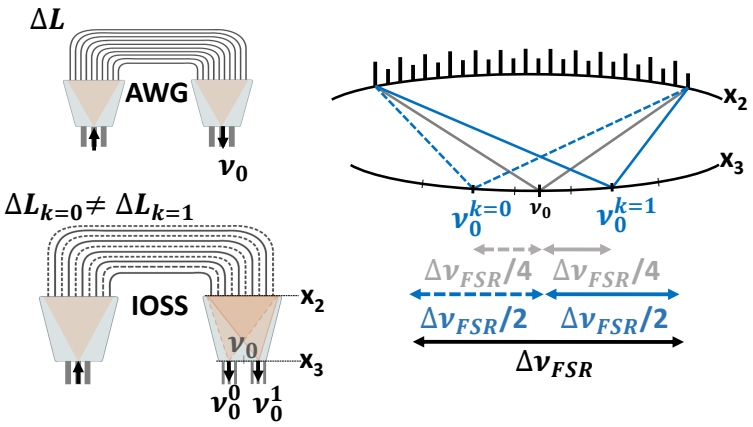

Figure 3.2: Graphical example of IOSS sub-arrays central frequency definition (with $M = 2$) based on a conventional AWG.

where w_g represents the light mode field radius at the AWs, M is the number of sub-arrays, N is the total number of AW, r is the number of the AW, and d_w the separation between AWs at planes X_1 and X_2 (Fig. 3.1-a). Symbol $*$ denotes the convolution operation, and $b_g(x_1)$ defines the field at each AW.

The terms in this equation can be regrouped and analysed separately to better understand their meaning. The expression $\sqrt[4]{2\pi w_g^2} B_i(x_1) \sum_{r=-\infty}^{+\infty} \delta(x_1 - Mrd_w - kd_w)$ stands for the amplitude of the field coupled at each AW, where the term $\delta(x_1 - Mrd_w - kd_w)$ determines the position of the waveguides of each sub-array. Likewise, the term $\prod\left(\frac{x_1}{Nd_w}\right)$ represents the truncation of the B_i function due to the limited number of arrayed waveguides.

The length of the different AWs of each sub-array is calculated as:

$$l_{r,k} = l_{c,k} + \Delta L_k \left(r + \frac{N}{2M}\right) + l_s + \Delta l_s \left(r + \frac{N}{2M}\right), \tag{3.5}$$

where $l_{c,k}$ is the length of the shortest waveguide of each sub-array, and ΔL_k is the incremental length for each sub-array, as it was already mentioned, which is defined as [91]:

$$\Delta L_k = \frac{m_k\ c}{n_c\ \nu_0^k}. \tag{3.6}$$

The variable m_k is an integer number which represents the order of the sub-array (known as *grating order*). These diffraction orders are generated due to the discretization of the field imposed by the AW ($\ldots m-1,\ m\ ,\ m+1,\ldots$). ν_0^k (λ_0^k) is the sub-array central frequency (wavelength), and n_c is the effective refractive index of the propagating mode at the AWs. In a conventional AWG, the central frequency (also called *design frequency/wavelength*) is understood as the

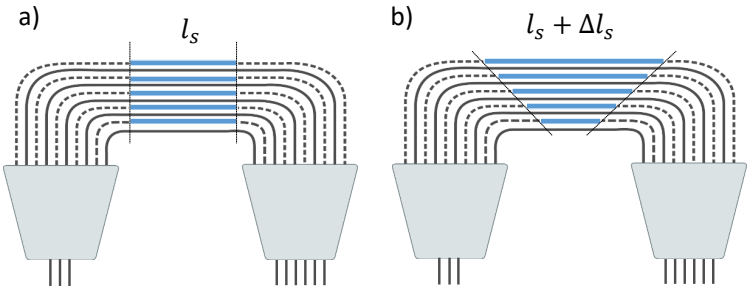

Figure 3.3: IOSS sensing windows configuration for **a)** Intensity interrogation and **b)** Wavelength/frequency interrogation.

light frequency which propagates from the centre of plane X_0 and focuses at the centre of X_3 plane (Figure 3.2). In the case of IOSS, each sub-array has its own central frequency, which position is designed to be shifted from the centre of plane X_3, as shown in Figure 3.2. The design frequency of each sub-array is obtained as:

$$\nu_0^k = \nu_0 + \left(k - \frac{M-1}{2}\right)\frac{\Delta\nu_{FSR}}{M} \tag{3.7}$$

where ν_0 and $\Delta\nu_{FSR}$ are the central frequency and Free Spectral Range in frequency of the conventional AWG on which the design is based.

The last two terms of Eq. (3.5) represent the waveguide section dedicated to detection purposes. As it was already mentioned in previous section, the configuration of the sensing windows depends on the interrogation method employed. Thus, the length will be kept constant if the analysis is based on intensity interrogation, while AW length will be incremental if the wavelength interrogation is performed (Figure 3.3).

Thus, the phase introduce by each AW can be calculated as:

$$\phi_{r,k}(\nu) = e^{-j\beta\left(l_{c,k}+\Delta L_k\left(r+\frac{N}{2M}\right)\right)}e^{-j\beta_k\left(l_s+\Delta l_s\left(r+\frac{N}{2M}\right)\right)}. \tag{3.8}$$

Since the extra waveguide sections are incorporated in both reference and sensing sub-arrays, the propagation constant β_k distinguishes propagation properties of both sets of arrayed waveguides (cover and exposed waveguides). Thus,

$$\begin{aligned} &\text{if } k \rightarrow \text{sensing sub-array:} \quad \beta_k = 2\pi n_{sens}\nu/c \\ &\text{if } k \rightarrow \text{reference sub-array:} \quad \beta_k = \beta = 2\pi n_c\nu/c \end{aligned} \tag{3.9}$$

where the variable n_{sens} represents the effective refractive index of the exposed waveguides when a sample is deposited on top of the chip. The propagation constant of the sensing sub-array will vary depending on the sample.

The phase difference between adjacent AW of the same sub-array is then given by:

$$\Delta\phi_k(\nu) = e^{-j\beta\Delta L_k} e^{-j\beta_k \Delta l_s}. \tag{3.10}$$

From this equation, it is clear that no phase change (and hence, no wavelength / frequency shift) is induced by the sample when the sensing sub-array is configured for intensity interrogation, since $\Delta l_s = 0$.

To obtain the expression of the field at plane X_2 it is enough to introduce the phase term (Eq. 3.8) in Eq. 3.4. After some mathematical simplification, the field at AWs output can be expressed as:

$$f_2(x_2,\nu) = \sqrt[4]{2\pi w_g^2}\cdot \\ \cdot \sum_{k=0}^{M-1}\left[\prod\left(\frac{x_2}{Nd_w}\right) B_i(x_2)\phi(x_2,\nu)\delta_{w,k}(x_2) e^{j\beta\Delta L_k\left(\frac{k}{M}\right)} e^{j\beta_k\Delta l_s\left(\frac{k}{M}\right)}\right] * b_g(x_2), \tag{3.11}$$

where each term is defined as:

$$\delta_{w,k}(x_2) = \sum_{r=-\infty}^{+\infty} \delta(x_2 - Mrd_w - kd_w), \tag{3.12}$$

$$\phi(x_2,\nu) = \varphi_k(\nu)\ \psi_k(\nu) e^{-j(\beta\Delta L_k + \beta_k\Delta l_s)\frac{x_2}{Md_w}} \tag{3.13}$$

where,

$$\psi_k(\nu) = e^{-j\beta\left(l_{0,k} + \Delta L_k \frac{N}{2M}\right)}, \tag{3.14}$$

and

$$\varphi_k(\nu) = e^{-j\beta_k\left(l_s + \Delta l_s\left(r + \frac{N}{2M}\right)\right)} \tag{3.15}$$

Finally, the field distribution at plane X_3 is obtained from the spatial Fourier transform of Eq. (3.11):

$$f_3(x_3,\nu) = \mathcal{F}\{f_2(x_2,\nu)\}\Big|_{u=\frac{x_3}{\alpha}} = \sqrt[4]{2\pi w_g^2} B_g(x_3)\cdot \\ \cdot \sum_{k=0}^{M-1}\left[sinc\left(Nd_w\frac{x_3}{\alpha}\right) * b_i(x_3) * \Phi(x_3,\nu) * \Delta_{w,k}(x_3)\cdot e^{j(\beta\Delta L_k + \beta_k\Delta l_s)\left(\frac{k}{M}\right)}\right] \tag{3.16}$$

where each term is obtained as:

$$B_g(x_3) = \mathcal{F}\{b_g(x_2)\}\Big|_{u=\frac{x_3}{\alpha}} = \sqrt[4]{2\pi w_g^2} e^{-\left(\pi w_g \frac{x_3}{\alpha}\right)^2}, \tag{3.17}$$

$$b_i(x_3) = \mathcal{F}\{B_i(x_2)\}\Big|_{u=\frac{x_3}{\alpha}} = \sqrt[4]{\frac{2}{\pi w_i^2}} e^{-\left(\frac{x_3}{w_i}\right)^2}, \tag{3.18}$$

$$sinc\left(Nd_w\frac{x_3}{\alpha}\right) = \mathcal{F}\left\{\prod\left(\frac{x_2}{Nd_w}\right)\right\}\Big|_{u=\frac{x_3}{\alpha}}, \tag{3.19}$$

$$\Phi(x_3,\nu) = \mathcal{F}\left\{\phi(x_2,\nu)\right\}\Big|_{u=\frac{x_3}{\alpha}} = \varphi_k(\nu)\ \psi_k(\nu)\delta\left(x_3 + \frac{\alpha\left(n_c\Delta L_k + n_{sens}\Delta l_s\right)}{Md_wc}\nu\right), \tag{3.20}$$

$$\Delta_w(x_3) = \mathcal{F}\left\{\delta_{w,k}(x_2)\right\}\Big|_{u=\frac{x_3}{\alpha}} = \frac{1}{M}\sum_{r=-\infty}^{+\infty} e^{-j2\pi k d_w\frac{x_3}{\alpha}}\delta\left(x_3 - r\frac{\alpha}{Md_w}\right). \tag{3.21}$$

Then, Eq. (3.16) can be rewritten as:

$$\begin{aligned} f_3(x_3,\nu) = \sqrt[4]{2\pi\frac{w_g^2}{\alpha^2}}B_g(x_3)\frac{1}{M}\cdot \\ \cdot\sum_{k=0}^{M-1}\Bigg[\psi_k(\nu)\varphi_k(\nu)e^{j(\beta\Delta L_k+\beta_k\Delta l_s)\left(\frac{k}{M}\right)} \\ \sum_{r=-\infty}^{\infty} e^{-j2\pi r\frac{k}{M}} f_M\left(x_3 - r\frac{\alpha}{Md_w} + \frac{\alpha\left(n_c\Delta L_k + n_{sens}\Delta l_s\right)}{Md_wc}\nu\right)\Bigg]. \end{aligned} \tag{3.22}$$

in which the function f_M stands for:

$$f_M(x_3) = b_i(x_3) * sinc\left(Nd_w\frac{x_3}{\alpha}\right). \tag{3.23}$$

The complete IOSS operation is described in Eq. (3.22). From the terms within function f_M, one can see that the focusing position of the field at the output of the second FPR (plane X_3, Figure 3.1-b), is determined by the number of sub-arrays M, the length increment between AW, ΔL_k and Δl_s, as well as the effective refractive index of the sensing waveguides, n_{sens}.

The second term of function f_M in Eq. (3.22), defines the Spatial Free Spectral Range (SFPR), which expresses the replication of the set of frequencies composing the input beam along plane X_3:

$$\Delta x_{3FSR} = \frac{\alpha}{Md_w}. \tag{3.24}$$

Variables conforming third term define the *Frequency-Spatial Dispersion Parameter* (FSDP) expressed as γ, which describes the offset and focusing of each frequency of light at different positions along plane x_3:

$$\gamma = \frac{Md_wc}{\alpha\left(n_c\Delta L_k + n_{sens}\Delta l_s\right)} \tag{3.25}$$

In the final stage, the field at the output waveguides is calculated as the overlap integral between the diffracted light at plane X_3, Eq. (3.22), and the fundamental mode of the output waveguides $b_o(x_3)$:

$$t_{0,q}(\nu) = \int_{-\infty}^{+\infty} f_3(x_3, \nu) b_o(x_3 - q d_o) \partial x_3, \tag{3.26}$$

being q the output waveguide number and d_o the output waveguides spacing (Figure 3.1-b).

Arbitraty Input Waveguide.

So far, a single centred input waveguide has been taken into account, however the formulation can be easily rewritten to consider any input waveguide position. Thus, the expression of the field at plane X_0 can be rewritten as:

$$b_{i,p}(x_0) = \sqrt[4]{\frac{2}{\pi w_i^2}} e^{\left(-\frac{x_0 - p d_i}{w_i}\right)^2} = b_i(x_0 - p d_i), \tag{3.27}$$

where p represents the position of the input waveguide, and d_i the input waveguides spacing. Taking this into account, the expression of the field at the output plane X_3 can be expressed as:

$$\begin{aligned} f_3(x_3, \nu) = \sqrt[4]{2\pi \frac{w_g^2}{\alpha^2}} B_g(x_3) \frac{1}{M} \cdot \\ \cdot \sum_{k=0}^{M-1} \left[\psi_k(\nu) \varphi_k(\nu) e^{j(\beta \Delta L_k + \beta_k \Delta l_s)\left(\frac{k}{M}\right)} \right. \\ \left. \sum_{r=-\infty}^{\infty} e^{-j2\pi r \frac{k}{M}} f_M \left(x_3 + p d_i - r \frac{\alpha}{M d_w} + \frac{\alpha \left(n_c \Delta L_k + n_{sens} \Delta l_s \right)}{M d_w c} \nu \right) \right]. \end{aligned} \tag{3.28}$$

The field at the output waveguides is then given by

$$t_{p,q}(\nu) = \int_{-\infty}^{+\infty} f_{3,p}(x_3, \nu) b_o(x_3 - q d_o) \partial x_3, \tag{3.29}$$

3.3 Design procedure

The very first step on the design procedure is to select the operating wavelength range of our device or application, as well as the suited fabrication platform for it. These concepts will determine the *Physical Parameters* of the design, which are the fundamental waveguiding parameters:

- Design central frequency (ν_0),

- FPR and arrayed waveguides refractive indexes (n_s and n_c, respectively) and
- Waveguides width (W_x) and modal field radius (w_x) of the propagating mode. The subscript x will be replaced by i and w to refer to input/output waveguides and arrayed waveguides, respectively.

Following, the basic design parameters (known as *High Level Parameters*) are settled taken into account the application requirements. These are:

- Number of channels (N_v),
- Frequency channel spacing ($\Delta\nu_{ch}$), which defines de difference in frequency between adjacent channels,
- Channel bandwidth ($\Delta\nu_{bw}$), which delimits the range of frequencies transmitted by each channel, and
- Loss non uniformity (L_u), which determines the amplitude signal ratio between the central and most external output waveguide.

The IOSS design steps have been compiled into the flow chart shown in Figure 3.4. This is an iterative process, since when the final step is reached, the result may not be the one expected or further improvements can be applied. The diagram arrows indicate the points in the process that can be retaken to apply changes in the design. These steps/parameters have considerable weight in the final response of the device. This section is structured according to the design flow.

3.3.1 Readout Scheme: Output Waveguides Distances

IOSS read-out scheme presents two possible configurations depending on the interrogation method employed. As discussed already, when frequency/wavelength interrogation is performed, a frequency/wavelength shift is translated into a focal point displacement along X_3 plane. In consequence, several output waveguides are necessary to track the focal point trajectory. On the contrary, during intensity interrogation, only the amplitude of the channels is affected, so a single output waveguide is needed. For all that, the most limiting factor in the design of the IOSS is given by the position of the output waveguides for the wavelength interrogation configuration.

In order to monitor the displacement of the focal point, the read-out system is composed by a set of three output waveguides for each sensing channel. In Figure 3.5, it is shown a diagram of the position of the different IOSS focal points (channels) for reference and sensing sub-arrays, as well as the output waveguides. It must be emphasized that this design example works with two sub-arrays ($M = 2$), but the results presented bellow can be easily extrapolated to larger M numbers. The gap between output waveguides dedicated to the same channel, d_A, needs to be short enough to capture the frequency shift. Likewise, external waveguides from adjacent channels must be far enough apart (d_B) to meet the application target crosstalk.

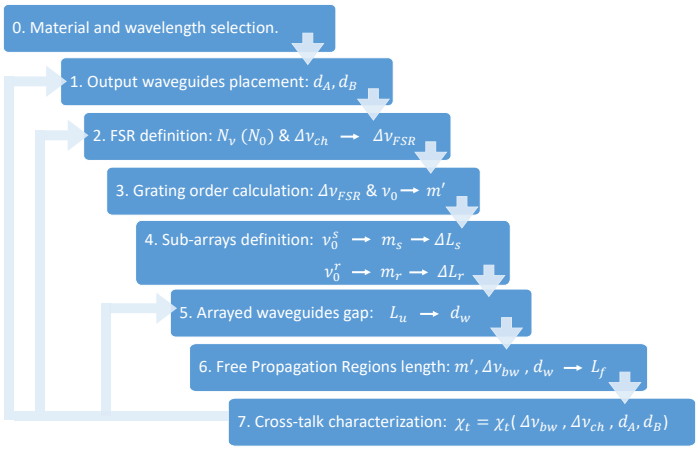

Figure 3.4: IOSS design flow. Step (0) Technology platform and wavelength range to work with depending on application. Step (1) Number of channels determination and corresponding output waveguides placement. Step (2) Free spectral range (FSR) in frequency definition based on N_ν and $\Delta\nu_{ch}$. Step (3) Calculation of the grating order of the AWG in which the IOSS is based. Step (4) Sub-arrays definition: central wavelength and incremental length calculation. Step (5) AW spacing determination from the parameter L_u. Step (6) Free propagation regions (FPR) length calculation. Step (7) Crosstalk characterization from the device response.

Consequently, d_A distance is fixed at the point where the output power of the signal from the centred waveguide decays $-3\ dB$. This is a reference value, but other criteria may apply. The field at a input/output waveguide was defined in Eq. 3.1. Applying the selected power decay ratio in this equation, the distance d_A is given by:

$$d_A = \sqrt{\frac{\ln 2}{2}} w_i. \tag{3.30}$$

Regarding distance d_B, the power decay is defined respect to the adjacent channel central signal. On this ocassion, a -10 dB power decay is settled. By applying again this criterion to Eq.3.1, the result is:

$$d_B = \sqrt{10^{(10/20)}} w_i. \tag{3.31}$$

Both equations are dependent with the mode field radius, w_i, which depends on the propagating frequency, cross-section of the waveguide selected and its materials (technology platform). It must kept in mind at all times the limitations imposed by the foundry due to fabrication (minimum distances between waveguides, minimum widths, bend radius, etc.), as this can severely restrict our design options.

The total distance between adjacent channels is then calculated as (Figure 3.5):

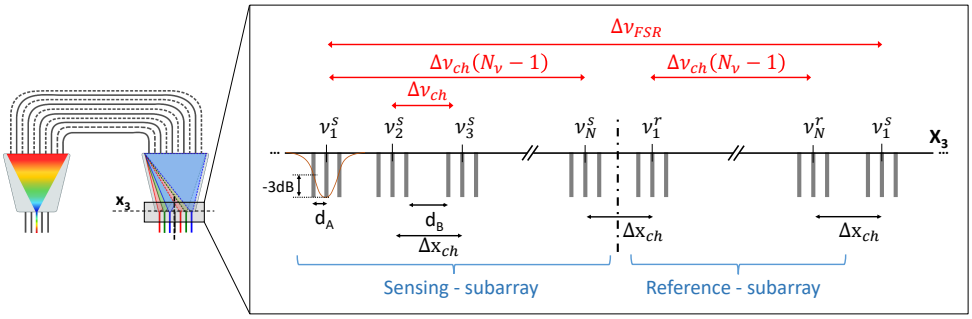

Figure 3.5: Diagram of IOSS FSR response, channels and output ports location at output plane x_3.

$$\Delta x_{ch} = 2d_A + d_B. \tag{3.32}$$

3.3.2 Readout Scheme: Optical Frequencies

The second step of the flow chart (Figure 3.4) is the definition of the Free Spectral Range (FSR) of the device. For that, the number of channels, N_v, and the channel bandwidth, $\Delta\nu_{ch}$, must have been previously defined according to the frequencies/wavelengths of interest to study the sample.

Following the scheme of Figure 3.5, the FSR of the device can be calculated as function of the number of sub-arrays (M) selected, which determine the number of channel replications:

$$\Delta\nu_{FSR} \geq M\Delta\nu_{ch}N_\nu. \tag{3.33}$$

In the example shown in Figure 3.5, M has been set to 2 for simplification (sensing and reference sub-arrays).

Next step in the design is the grating order calculation. The relation between the grating order and the Free Spectral Range is given by [68,91]:

$$m' = \frac{\nu_0}{\Delta\nu_{FSR}} \tag{3.34}$$

However, this expression does not take into account the waveguide dispersion. Hence, the modified grating order (m) is employed, in which the effective index and the group index are considered:

$$m = \left\lfloor \frac{n_c}{n_g} m' \right\rfloor = \left\lfloor \frac{n_c}{n_g} \frac{\nu_0}{\Delta\nu_{FSR}} \right\rfloor. \tag{3.35}$$

This expression is employed to obtain the grating order of the AWG in which the IOSS is based, as well as the grating orders of the sub-arrays:

$$m^s = \left\lfloor \frac{n_c}{n_g} \frac{\nu_0^s}{\Delta\nu_{FSR}} \right\rfloor and \tag{3.36}$$

$$m^r = \left\lfloor \frac{n_c}{n_g} \frac{\nu_0^r}{\Delta\nu_{FSR}} \right\rfloor, \tag{3.37}$$

where the superscripts s and r stand for sensing and reference sub-arrays respectively.

In turn, the optical central frequencies for the sub-arrays are calculated by combining Eq. 3.7 and Eq. 3.33:

$$\nu_0^s = \nu_0 - \frac{\Delta\nu_{ch} N_\nu}{2}, \tag{3.38}$$

$$\nu_0^r = \nu_0 + \frac{\Delta\nu_{ch} N_\nu}{2}. \tag{3.39}$$

Finally, the corresponding incremental length for each sub-array can be determined by directly replacing the obtained grating order and central frequencies values in Eq. 3.6.

3.3.3 Focusing and Periodicity: Arm spacing and FPR length

In the next two design steps, the distance between arrayed waveguides (d_w) and the FPR length (L_f) of the IOSS are set. For that, the high level parameters L_u and $\Delta\nu_{bw}$ are linked with the parameters obtained in previous steps.

In a conventional AWG, both d_w and L_f are calculated based on the selected central frequency ν_0. In the case of IOSS, although two different central frequencies have been defined, both are related to ν_0. In this way, the values of d_w and L_f can be later obtained to define a common FPR to both sub-rays.

The expressions employed in the calculus of d_w and L_f follow the same formulation than for a conventional AWG, which can be reviewed in [68,91]. Because of this, only the most relevant equations are reproduced in this section.

The diffracted light reaching IOSS ouput plane (X_3) has a non-uniform power distribution due to $B_g(x_3)$ in Equation 3.22, which maximum is at the centre of the plane and decays towards the sides. The power relation between the central and most external output waveguides is defined by the loss non-uniformity parameter (L_u). The value of L_u is settled by the designer taking into account a trade-off: L_u lower values will provide a flat response between IOSS channels, but will produce high secondary lobes at the output signal.

The distance between AW (d_w) in planes X_1 and X_2 is related to L_u through the following formula [68]:

$$d_w = \frac{w_w \ \pi \ m \ \Delta\nu_{ch} \ N_\nu}{\nu_0} \left[ln\left(10^{\frac{L_u(dB)}{20}}\right) \right]^{-\frac{1}{2}}. \tag{3.40}$$

In turn, the channel bandwidth ($\Delta\nu_{bw}$) will determine the length of the FPR. $\Delta\nu_{bw}$ is defined at the Full Width at Half Maximum (FWHM) of the output waveguide passband, and it is predefined by the designer. In Eq. (49) from [68] the relation between these two parameters is presented, from which the value of L_f can be derived:

$$\Delta\nu_{bw} = 2\gamma w_i \sqrt{2\,ln\left(10^{3/20}\right)} = 2\frac{d_w\ \nu_0^2\ n_s}{m\ c\ L_f} w_i \sqrt{2\,ln\left(10^{3/20}\right)}, \tag{3.41}$$

where n_s is the refractive index of the FPRs.

The device layout uses a regular Rowland mounting for the FPRs, which is defined by the L_f and d_w calculated above, employing the parameters of the AWG in which the design is based. This is a compromise approximation, since the IOSS two sub-arrays may not be perfectly focused. To optimize the focusing features of each sub-array independently, other mounting configurations could be investigated [94].

Once the parameters of the FPR are set, the number of arrayed waveguides (N) is calculated. For that, the designer has previously established the Array Acceptance Factor (AAF), which determines the power percentage of the diffracted signal that is captured by the AW. The calculation is done iteratively, increasing the number of guides by two and calculating the power integral in each iteration until the target AAF is reached.

Following all the steps described above, the IOSS spectral response is achieved. However, the due to some fabrication limitations, as the lithografic resolution, the experimental result may not fulfill completely the input design parameters. In this case, the design must be iterated, and this is highlighted for steps 1, 2 and/or 5 in the design flow of Figure 3.4.

3.4 Reference Designs

In this section, two IOSS reference designs are presented conceived as self-reference absorption spectrometers. Both devices are then configured for intensity interrogation, what in terms of design implies that: i) only one output waveguide per channel is necessary, and ii) all the sensing windows have the same length. The devices have been designed for particular applications at the visible (VIS) and near-infrared (NIR) wavelength ranges, respectively. The application of the first design is in the field of the food quality control, to determine the concentration of a particular dye in aqueous solution. The second device is applied in the quality control of alcoholic beverages.

Regarding design, both devices have been configured with two sub-arrays in the most compact configuration, which mathematically is expressed as $\Delta\nu_{FSR} = 2\Delta\nu_{ch}N_\nu$. This implies that the channels of the two sub-arrays are periodically interleaved, with a spectral separation of $\Delta\nu_{ch}$ between sensing and reference channel sets (as shown in Figure 3.5).

The steps for simulating the device responses are explained below. Firstly,

for each waveguide cross-section employed in the design (straight, bend, slab and sensing waveguides), the effective refractive index and the propagation mode field of propagating light is calculated. This is done using a mode solver software, in which the data of the technology used are loaded. Naturally, both devices are based on the silicon nitride on silica (Si_3N_4/ SiO_2) technology [89]. Secondly, all the parameters of the device are settled and calculated following the design flow described in Section 3.3. Next, the layout of the IOSS is built employing OptoDesigner tool from Synopsys [84]. All the design parameters together with the length of each AW are then exported to simulate the response of the device in Matlab, following the formulation presented in Section 3.2.

3.4.1 Visible Wavelength Range Device

The IOSS device described in this section is designed for determining the concentration of the Sunset Yellow (SY) coloring dye (additive E-110), employed commonly in the food industry [95], as well as in drugs and cosmetics. Below certain concentration levels, these dies are not harmful to the human being. The absorption spectra of SY dye is well known for different concentrations [96] in the VIS range, presenting prominent peaks between 470 and 520 nm wavelengths.

Based on this data, the IOSS central wavelength is set to $\lambda_0 = 495$ nm. The height of the substrate buried oxide (BOX) and cladding layers are 2μm and 1.5 μm, respectively. The Si_3N_4 waveguide core is designed with a cross-section of 400 nm width and 100 nm height, and the bend radius employed is 35 μm. These specifications ensure single-mode and single polarization (TE) waveguides behaviour in the targeted spectral range. The simulated effective refractive index for strip and slab waveguides are n_c (λ= 495 nm) = 1.6582 and n_s (λ = 495 nm) = 1.9976, respectively. The calculated group index for λ = 495 nm is n_g = 2.1114. The channel wavelength spacing is fixed to $\Delta\lambda_{ch} = 2$ nm, which results in a $\Delta\nu_{FSR} = 19.57$ THz and, therefore, a diffraction order $m = 24$. To minimize the cross-talk, the AW spacing and the channel bandwidth are settled to $d_w = 1.2$ μm and $\Delta\nu_{bw} = 0.2\Delta\nu_{ch}$. From these values, the FPR length is deduced to be L_f = 95.91 μm.

In order to sample the decay of the SY absorption peak (Figure 2 from [96]), we decided to analyse the following four wavelengths: $\lambda_1 \approx 476$ nm, $\lambda_2 \approx 488$ nm, $\lambda_3 \approx 502$ nm and $\lambda_4 \approx 515$ nm. Although the channel wavelength spacing was set to 2 nm, these target wavelengths can still be analysed due to the spectral periodicity of AWG (IOSS) devices, by studying adjacent diffraction orders.

The absorption values as function of the SY concentration employed in this simulation were taken from Figure 2 of reference [96]. Knowing the absorption levels on the target sample and the percentage of evanescent field in contact with it (18%), the length of the sensing windows was set to 200 μm.

In Figure 3.6, the spectral response of the eight channels (4 channels × 2 replications) are represented for lower (a) and higher (b) SY concentrations. The spectral responses have been plot separately (1–4 and 5–8) so that the duplication of channels (1–5, 2–6, 3–7 and 4–8) can be easily examined. In these simulations,

a flat spectral broadbandsignal is defined as input source, for illustration purposes. Nonetheless, the characterization of this design must be done employing narrow band light sources centered around the wavelengths of interest to avoid the overlap between adjacent channels.

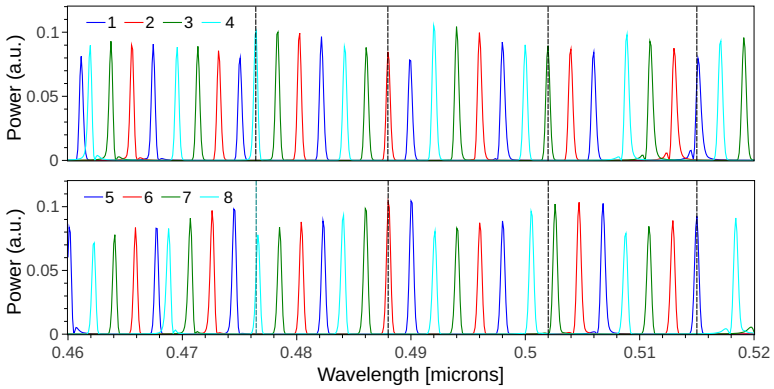

(a) SY $C = 0.2$ mM

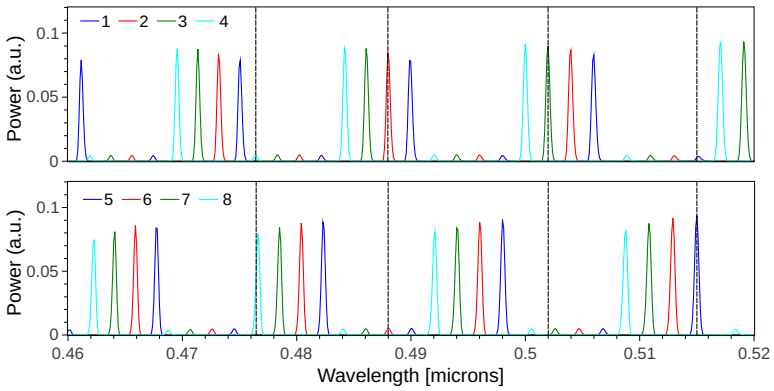

(b) SY $C = 11.0$ mM

Figure 3.6: IOSS spectral response for channels 1–8 for sunset yellow (SY) concentrations (**a**) $C = 0.2$ mM and (**b**) $C = 11.0$ mM. Channels are colored in pairs, with same color for those having spectrally aligned responses. The dark dashed vertical lines correspond to the targeted wavelengths 476, 487, 502 and 515 nm.

By contrasting Figures 3.6-a and 3.6-b, the variation in intensity due to the absorption of the sample can be clearly observed. Likewise, the contributions of the reference and sensing sub-rays are evidenced. From each output, contributions from both reference and sensing sub-arrays are acquire. For example, looking at 3.6-b, channel 2 and channel 6 show, for λ =488 nm, the contributions from

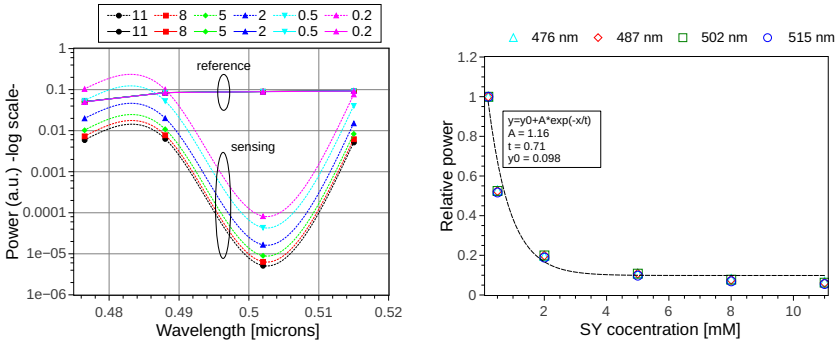

(a) Reference and sensing channel spectra (b) Relative power vs. concentration

Figure 3.7: (**a**) Reference and sensing channel spectra for the targeted wavelengths 476, 487, 502 and 515 nm, with reference channels (solid lines) and sensing channels (dashed lines) for different SY concentrations. The values are interpolated using smoothed (spline) lines. (**b**) Relative power change with respect of the starting concentration (C = 0.2 mM) for the four targeted wavelengths.

the reference and sensing sub-arrays, respectively. However, for λ =476 nm, the contribution of the sensing sub-array is shown in channel 4 and reference in channel 8. The exchange of the sensing and reference contributions is due to the sub-arrays interleaving. It should be noted that the analysed wavelengths fall within different FSR of the device response. Therefore, one can strictly refer output signals as reference/sensing channels when a single FSR of the response is analysed. This is only relevant in the power ratio calculation P_s/P_r, for which the proper readout signal needs to be assigned to each. Another point to highlight from Figure 3.6 is that sensing and reference channels are not exactly equally spaced in wavelength, which is due to the average L_f parameter employed, as described in Section 3.3.3.

The simulations were performed for SY concentrations ranging from 0.2 to 11.0 mM in aqueous solution. The resulted spectral response of the analysed wavelengths is shown in Figure 3.7. In Figure 3.7-a the power of the sensing (dashed lines) and reference (continuous lines) channels is plotted for the target wavelengths. As it can be observed, power of reference channels do not vary with concentration, as it was expected, since reference AW are not in contact with the sample. On the contrary, the sensing channels perfectly reflect the variation in power as a function of sample absorption. For SY die case, the higher the concentration of the sample, the higher the absorption and, therefore, the lower the signal power is detected. The intensity profile acquired is in agreement with the absorption spectra of Figure 2 from reference [96], as it was expected. The evolution of the sensing and reference power ratio for the four target wavelengths is shown in Figure 3.7-b, taking the power ratio for C = 0.2 mM as reference. From this graph, a similar relative power variation with respect concentration is observed

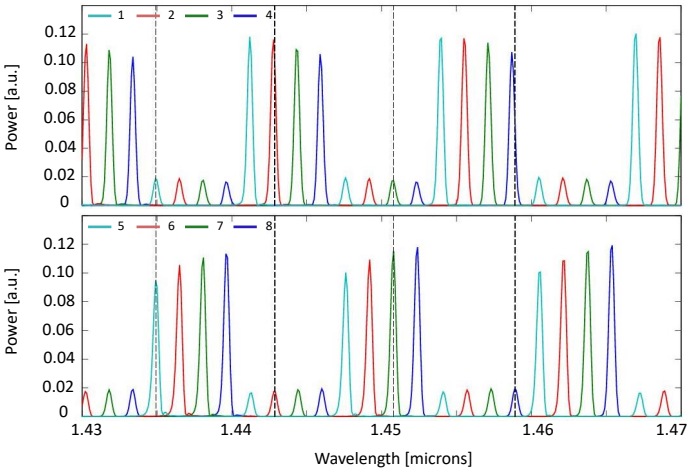

Figure 3.8: IOSS spectral response for channels 1–8 for ethanol concentrations (a) $C =$ 20 wt %. Channels are colored in pairs, with same color for those having spectrally aligned responses. The dark dashed vertical lines correspond to the targeted wavelengths 1435, 1443, 1451 and 1459 nm.

for the wavelength studied. This indicates that, based on a previous calibration of the sensor, the concentration of the sample can be stablish.

3.4.2 Near Infrared Device

The IOSS device has been also applied as an absorbance sensor in the NIR wavelength range. In this example, the device employed for measuring ethanol concentration in solution. A direct application for this device can be in the food quality control area, specifically in the determination of alcohol in spirituous liquors [97].

The data employed to simulate the response of the device is taken from [98], where several samples of ethanol and water solutions are analysed at different ethanol concentrations. From this data, we decided to perform the intensity analysis as function of the concentration at wavelengths around 1450 nm, where the ethanol–water mixture presents an absorption peak. Hence, the central wavelength of our device was settled to $\lambda_0 = 1450$ nm. The design process was the same as discussed previously. For NIR application, the BOX layer height was set to 3 μm, while keeping 1.5 μm height for the cladding layer. For single-mode configuration, the core waveguide cross-section were set to 800 nm$\times$ 300 nm (W $\times$ H), and a bend radius R =75 μm was employed. The values of the refractive indexes simulated in this model were: n_c (λ= 1450 nm) = 1.5702, n_g (λ= 1450 nm) = 1.9314, and n_s (λ = 1450 nm) = 1.6757. The four target wavelengths chosen for the ethanol concentration analysis were (approximately) 1435, 1443, 1451 and 1459 nm. We settled $\Delta\lambda_{ch} = 1.6$ nm, which results in $\Delta\nu_{FSR} = 1.824$ THz and, therefore, a diffraction

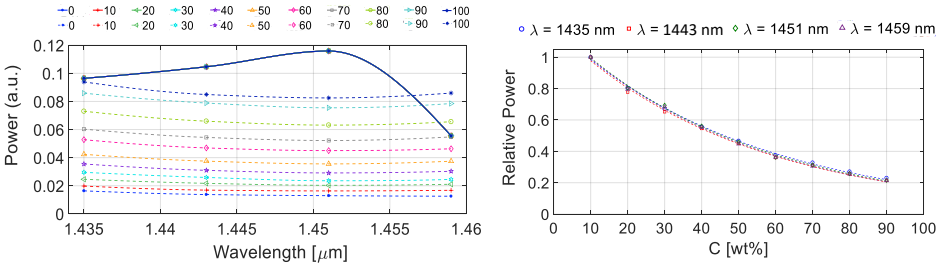

(a) Reference and sensing channel spectra

(b) Relative power vs. concentration

Figure 3.9: (**a**) Reference and sensing channel spectra for the targeted wavelengths 1435, 1443, 1451 and 1459 nm, with reference channels (solid lines) and sensing channels (dashed lines) for different ethanol concentrations [0–100 wt %]. The values are interpolated using smoothed lines. (**b**) Relative power change with respect of the starting concentration ($C = 10$ wt %) for the four targeted wavelengths.

order m=92. Lastly, the $d_w = 3$ μm determines a FPR length of 158.47μm.

The spectral response (in terms of IOSS operation) is very similar to that the one already shown for VIS IOSS design (Figure 3.7). For this reason, only the spectral response for low ethanol concentration ($C = 20wt\%$, given in mass fraction) is shown in Figure 3.8 as verification. Then, the absorption spectrum is derived following the same procedure as in the previous example. In Figure 3.9-a, the power measured at the four target wavelengths is plotted for ethanol concentrations ranging from 0 $wt\%$ to 100 $wt\%$ in ethanol-water solutions. Dashed and continuous lines represent the measurements from the sensing and reference channels, respectively. As expected, the signal power of reference channels signal remains unchanged, while the sensing channels power is reduced as the ethanol mass fraction percentage increases. As done for the data from previous example, in Figure 3.9-b is represented the relative power variation with the concentration, referenced to the lower concentration (C = 10 wt %).

These results show a more subtle concentration-dependent change in power compare to the previous example (Figure 3.7-a). This suggests that the sensing area can be further optimized to improve the IOSS operation, which can de done either incrementing the sensing path length, or modifying the waveguide cross-section to achieve higher interaction of the evanescent field with the sample. Regarding this concept, a simulation with different sensing path lengths (L_{IOSS} = 400–3000 μm) was performed, analysing the performance of the device in the four target wavelengths employed for ethanol concentration analysis. Since the results were similar for the four of them, only the outcome for $\lambda = 1435$ nm is shown in Figure 3.10 to avoid repetition. As it can be appreciated, output power from sensing channels (P_{sens}) is nearly zero for low concentrations, and large L_{IOSS} worsen the result. The suited L_{IOSS} for the waveguide cross-section defined above would be 900 μm, since is the one presenting the larger slope (which means higher sensor

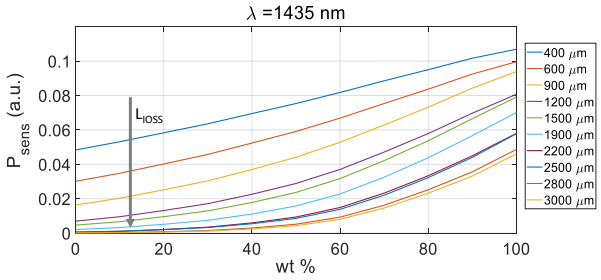

Figure 3.10: IOSS output power at the sensing channel $\lambda = 1435$ nm for sensing path lengths from 400 μm to 3000 μm. The arrow shows the incremental trend of the sensing path.

sensitivity), while P_{sens} is still measurable for low concentrations.

3.5 Conclusions

As conclusions, a brief summary of the chapter contents and the achieved goals follows. The general objective of this chapter is to introduce a novel spectroscopic sensor architecture based on a modified AWG (DI-AWG). The concept, mathematical model and design procedure of the sensor have been described. The reported model details the operation of the device in its two possible configurations (intensity and wavelength/frequency interrogation). From the mathematical model, the design procedure is derived. Once the high level parameters are specified, all the necessary parameters to draw the device layout are obtained. Both formulation and design modelling follow a similar procedure as a conventional AWG, with the particularity of the sub-array definition and the sensing windows configuration. Including both reference and sensing signals in a single device results into a more direct measurement of the sample to be analysed. Besides, the device footprint is reduced when compared to parallel architectures with demultiplexing and sensing in a single device. In addition, two IOSS design examples are provided working at VIS and NIR wavelength ranges to show the versatility of the design and, thus, of the device. The use of this proposed device to different applications is possible by selecting a proper combination of integrated technology, detectors and light sources.

The results obtained through this chapter have been reported in the following publications:

- G. Micó, B. Gargallo, D. Pastor, P. Muñoz, “Integrated Optic Sensing Spectrometer: Concept and Design”, *Sensors*, vol. 19, no. 1018, 2019.
- P. Muñoz, B. Gargallo, G. Micó, D. Pastor,“Dispositivo Fotónico Sensor, Método de análisis de muestras que hace uso del mismo y usos de dicho dispositivo”, ES Patent OEPM P201,631,544.

- G. Micó, D. Pastor, P. Muñoz, "Optical spectroscopic sensor based on a novel Arrayed Waveguide Grating configuration " *XIV European Conference on Optical Chemical Sensors and Biosensors (Europtrode XIV)*, Naples, Italy, 25th - 28th March, 2018.
- G. Micó, B. Gargallo, D. Pastor, P. Muñoz, "Sensor espectroscópico integrado basado en un AWG intercalado" *XI Reunión Española de Optoelectrónica (OPTOEL 2019)*, Zaragoza, Spain, 3rd - 5th July, 2019.

Chapter 4
IOSS proof-of-concept

In this chapter, the proof of concept of the IOSS operating in the C-band wavelength range is presented. Several configurations of the device were designed and fabricated to progressively analyse the IOSS operation, as well as its ability to sense. The chapter is structured as follows: firstly, the IOSS proof-of-concept configured for intensity interrogation is reported in Section 4.1. In section 4.1.1, various IOSS and AWG design devices are described for their comparison and analysis, and their simulated responses are reported as well. Following, the characterization of the devices is presented is Section 4.1.2, where firstly the experimental setup employed for the characterization is described. Next, the experimental results obtained for each of the devices are shown and discussed. In Section 4.1.3, the IOSS sensing features are evaluated by depositing different samples on top of the chip and analysing the sensor response. Finally, in Section 4.2, further IOSS configurations designed to improve the operation of the sensor are reported. The chapter conclusions are given in Section 4.3.

4.1 Proof of concept

In this section, the IOSS experimental validation is presented. The device has been designed for the Si_3N_4 technology reported in Chapter 2, and fabricated through a Multi-Project Wafer (MPW) run. For the MPW run, the Buried Oxide (BOX) lower cladding is 2.5 μm height, the Si_3N_4 layer is 300 nm (for DEWVG cross-section) and the upper cladding layer (SiO_2) is 2.0 μm height. The Si_3N_4 oxidation and cladding Rapid Thermal Aniling (RTA) process steps have been applied to all the wafers of this run. The size of the manufacturing chip is 11×5.5 μm^2.

4.1.1 Design and simulation

The IOSS design is developed following the design procedure presented in Section 3.3. The center wavelength has been set to $\lambda_0 = 1550$ nm to take advantage

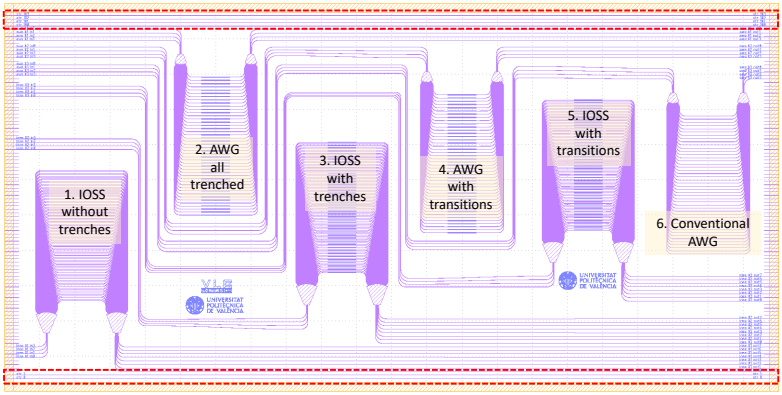

Figure 4.1: Chip layout containing the designs of conventional AWG and IOSS devices without sensing windows (1 and 6), implementing sensing windows (2 and 3) and implementing sensing windows together with transitions cladding/trench cross-sections (4 and 5). Red sections identify the straight waveguides test structures.

of all the characterization of the technology performed at this wavelength range. As in previous examples, the IOSS design consists of two sub-arrays ($M = 2$) employed for reference and sensing measurements respectively. To analyze the IOSS operation piecewise, three different designs within the same chip are made, departing from a base simplified case, and incorparting progressively the different ingredients to build the actual IOSS, as described below.

Figure 4.1 shows the chip layout with six structures: three AWGs and three IOSS devices. These designs are devised to compare each IOSS device with its corresponding AWG, having common design parameters, to discern the the effect of the sub-arrays definition. Thus, devices 1 and 6 correspond to a conventional AWG and an IOSS, respectively, including an extra length in the middle part corresponding with the sensing length. However, no sensing windows (trenched areas) are created in these sections. On the contrary, devices 2 and 3 contain also the sensing windows, in all the arrayed waveguides in the case of the AWG, and only in one of the sub-arrays, in IOSS case. Finally, a configuration has been introduced originally aimed at minimizing the losses and phase errors in the interface between covered and trenched waveguide cross-sections. Hence, devices 4 and 5 include transitions in such junctions. The structures selected by red dashed squares in Figure 4.1 are straight waveguides of 1 μm width employed as reference in the measurements. The source spectrum after traversing the straight waveguides is used to normalize the response of every device in the chip, since an ASE source is employed with non-flat spectral response. This also allows for compensating the in/out coupling losses to/from the chip.

The nominal waveguide width employed in the design is $W = 1\mu$m, with a bend

Device	W_{io} (μm)	W_{aw} (μm)	d_w (μm)	N_{in}	N_{out}	$\Delta\lambda_{ch}$ (nm)	$\Delta\lambda_{bw}$ (nm)	$\Delta\lambda_{FSR}$ (nm)	N	m	L_f (μm)	ΔL (nm)
AWG	2	1	3	4	4	1.6	0.4	12.8	45	99	151.017	97.34
IOSS	2	1	3	4	8	1.6	0.4	12.8	89	99/98	299.014	98.32/98.76

Table 4.1: AWG and IOSS devices main design parameters. Abbreviations: W_{io} stands for input/output slab waveguides width, W_{aw} for arrayed waveguides width, d_w for the distance between input/output waveguides, N_{in} for the number of input waveguides, N_{out} for the number of output waveguides, $\Delta\lambda_{ch}$ for the channel spacing, $\Delta\lambda_{bw}$ for the channel bandwidth, $\Delta\lambda_{FSR}$ for wavelength Free Spectral Range, N for the total number of arrayed waveguides (AWs), m for grating order, L_f for focal length, ΔL for incremental length between consecutive AWs. Note that for IOSS device two values for m and ΔL are given, one for each sub-array.

radius of $R = 75$ μm. The sensing windows are 400 μm long (l_s) and of 14 um width. The sensing length is constrained due to the limited chip surface, therefore it is not optimized for sensing a target analyte. The width of the waveguides within the sensing windows for designs 2 and 3 is kept to W_{tw} =1 μm. On the other hand, in devices 4 and 5, both covered and sensing waveguides were designed to maintain similar propagation properties, so the width of the sensing waveguides is set to W_{tw} =1.3 μm. The design parameters for the AWG and IOSS devices are summarized in Table 4.1. The footprint of the devices is 1190×2630 μm^2 for the AWGs and 1315×2650 μm^2 for IOSS.

The simulated responses for the devices pairs 1 – 6, and 2 – 3 are represented in Figure 4.2. In these simulations, the propagation losses of the technology are not included, therefore, the insertion losses shown in the graphs correspond to the diffraction losses of the device. IOSS presents larger insertion losses than the AWG, because now we have unfolded one focal point into two, by means of the two subarrays. In turn, the sensing waveguides are simulated on air, thus no losses due to sample absorption are considered. Because of this, there are no variations in the response of trenched and not-trenched devices. It is an expected result since it proves that sensing windows refractive index change (i.e., phase changes) do not affect the response of the device, because all the sensing windows have the same length. Hence, by applying the corresponding absorption/losses coefficient, only a change in power will be noticed. Therefore, the reponses from devices 4 and 5 (AWG and IOSS containing transitions sections between covered and trenched waveguides) have been omitted due to redundancy, as only the refractive index of the sensing guides varies respect to previous designs and, as explained, this does not affect the device response.

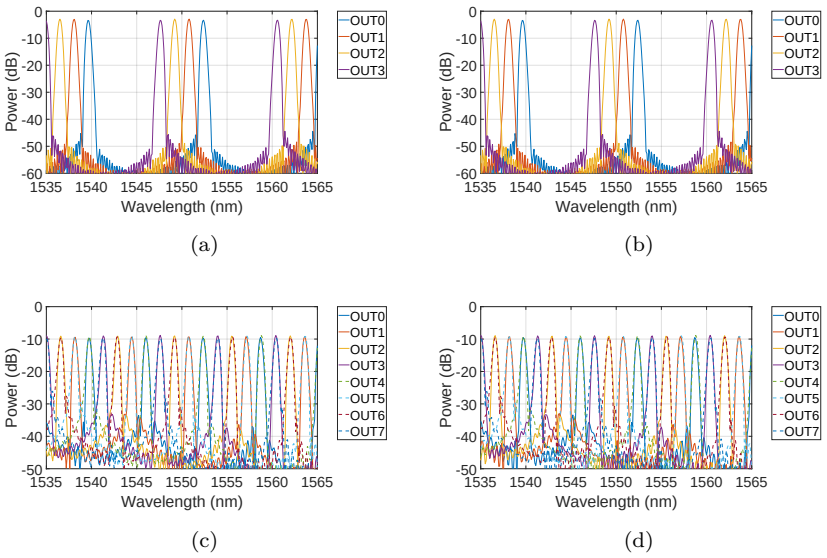

Figure 4.2: Simulated response of AWG without (**a**) and with (**b**) trenched waveguide sections, and IOSS device without (**c**) and with (**d**) trenched waveguide sections.

4.1.2 Characterization

Experimental setup

An sketch of the complete setup employed for the characterization of the chips is shown in Figure 4.3. The setup is mounted on top of an anti-vibration table, over three stations, each comprising different positioners with a variety of travel ranges and control mechanisms (manual, piezo-electric). The bare chip is hold using a vacuum chuck on top of a copper mount. The temperature of the sample has been kept to 25°C during the experiments using a thermoelectric cooler (TEC). A vision system (camera and monitor) is used as aid to help in the manual alignment steps of the measurements. We used microscope objectives on a setup that allows light to undergo polarization filtering coming from/to fibers, as described in Figure 4.3-b. For visual alignment, a red laser is employed. Once the alignment is achieved, an ASE broad band source is used. The output signal of the device is acquired by an OSA YOKOGAWA AQ6370C, with 10 pm resolution.

Experimental results

The obtained results are shown in Figures 4.4 and 4.5. All the spectral traces shown in the graphs are normalized to the average response of the straight waveguides, as mentioned before. All the analysis was performed for TE polarization,

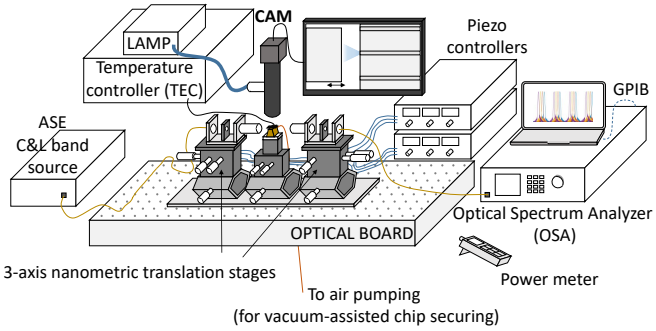

(a)

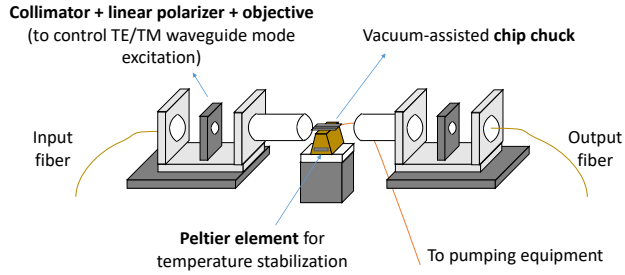

(b)

Figure 4.3: (**a**) Complete experimental setup sketch. (**b**) Input/output coupling stages.

so polarization filters are placed at both input and output of the chip. The light is coupled into the devices through one of the input centered waveguides (IN2) and the response from each output waveguide is acquired. In the first experiment, devices 1 and 6 are compared. As can be observed from Figure 4.4-a, the response of the AWG differs from the simulations previously shown. The AWG channels show high side lobes which are typically attributed to a combination of slab coupler phase non-linearity [99], phase errors [100, 101] and polarization rotation [102]. These were not compensated in design, since we wanted to introduce the minimum number of refinements, so as to have a basic proof-of-concept, with the less uncertainties incorporated. However, for IOSS, the experimental response (Figure 4.4-b), is quite similar to the simulated response (Figure 4.2-b). The uneven power distribution among channels, as compared to the simulations, can be attributed to the same effects discussed for the AWG. The FSR obtained from measurements is $\Delta\lambda_{FSR} = 12.84$ nm for AWG and $\Delta\lambda_{FSR} = 12.53$ nm for IOSS. In turn, the resulted wavelength channel spacing is $\Delta\lambda_{ch} = 1.56$ nm for AWG device and $\Delta\lambda_{ch} = 1.58$ nm for IOSS. All these values are in close agreement with the target design parameters given in Table 4.1.

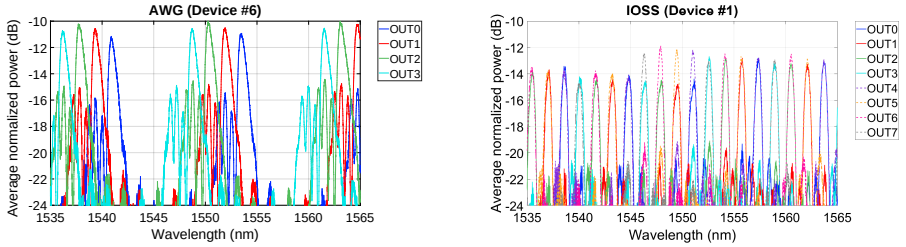

(a) (b)

Figure 4.4: Measurements of the AWG (**a**) and IOSS (**b**) devices without sensing windows.

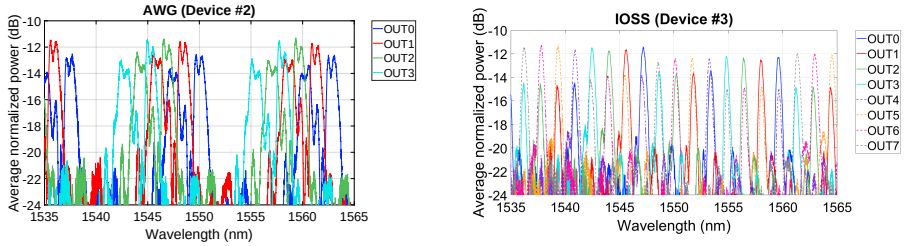

(a) (b)

Figure 4.5: Measurements of the AWG (**a**) and IOSS (**b**) devices with sensing windows.

Figure 4.5 shows the response for devices 1 and 2 (AWG and IOSS incorporating sensing windows). The $\Delta\lambda_{FSR}$ and $\Delta\lambda_{ch}$ are the same than in the previous designs for both AWG and IOSS. Nonetheless, the AWG response exhibits larger side lobes and thus insertion loss, than the preceeding design. Besides the aforementioned deleterious effects, that can be partially corrected by design, one should consider the transisitions to the trenched areas can introduce extra loss and unwanted reflections. The latter could be subject of design optimization as well.

Albeit all the above, a first evidence for the proof-of-concept is revelaed in this traces: an intensity variation is observed in IOSS (device #3) between reference and sensing channels. As explained in Section 3.4.1, from a single output, sensing and reference sub-array contributions are measured. For example, looking at OUT0 response (blue continous line, Figure 4.5-b), the spectral pass-bands at 1547 nm and 1560 nm present higer power than those at 1541 nm and 1553 nm. This constitutes a clear identification of sensing and reference bands, since larger losses are expected in the sensing AWs due to: i) higher propagation losses, since the propagating mode is more confined and thus, there is more interaction with side-walls, and ii) the aforementioned non-optimal transitions between cladded and trenched waveguides.

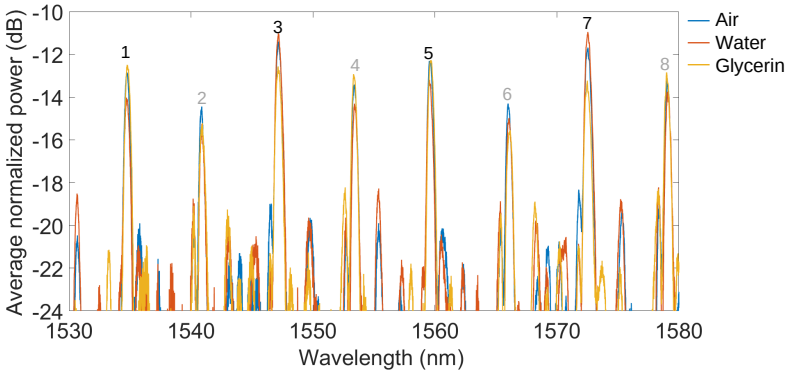

Figure 4.6: Spectral response measured from IN2/OUT0 input/output waveguides pair for the different samples analysed. The numbers specify the analysed spectral contributions from reference (1,3,5,7) and sensing (2,4,6,8) sub-arrays.

Finally, the spectral responses from AWG and IOSS (devices #4 and #5), a first attempt of optimization for the transitions in the cladded/trenched waveguides interfaces, showed barely defined channels. One possible reason may be that the sensing waveguides (whose width is W_{tw} =1.3 μm) have multi-mode behaviour, as opposed to what the simulations reported. Hence, if the transition is imperfect from a modal perspective, higher order modes can be excited, and they can create spurious spectral features in the end-to-end power transfer function.

4.1.3 Sensing measurements

In order to test the sensing attributes of the device, the spectrum of different samples is measured employing IOSS device #3. The substances used are distilled water and glycerin, which were selected due to their high absorption coefficient around 1550 nm wavelength [103, 104]. The measurements were performed employing the same experimental setup than presented in section 4.1.2. Once the device is characterised with no sample on it (sensing waveguides surrounded by air), a drop of the corresponding sample is deposited on top of the chip.

Two different experimental methodologies have been implemented. In the first experiment, the IOSS is characterised measuring the transmission signal from a single input (IN2) to all the output waveguides for each of the cases in this consecutive order: i) no sample over the chip, ii) distilled water (DH_2O) and iii) glycerine. To do so, the position of the output objective had to be changed to collect light consecutively from different output waveguides. When returning to the same output, for measurements of different samples, the optical coupling uncertainty is also included in the measurements. This makes a direct one to one comparison not possible, because the change due to different absorption coefficients is lower than the optical coupling uncertainty. This is shown in Figure 4.6. This in turn can be solved in a design for which there is sufficient length of trenched wavegui-

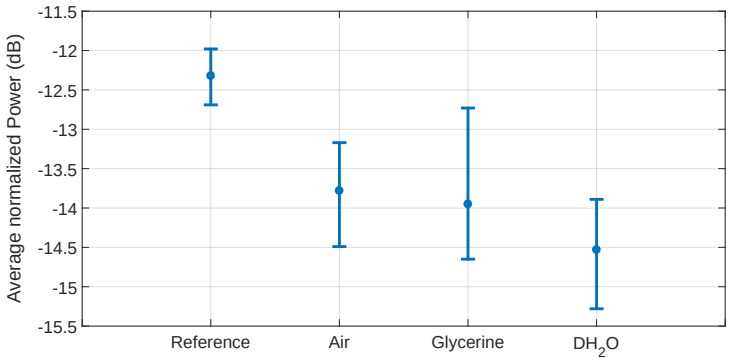

Figure 4.7: Average normalized power measured for the different cases/samples analysed.

des. However, as previously metioned, the present designs are not analyte-specific, and the sensing length was reduced so as to fit several layouts in the MPW fab run given chip area. To mitigate this variability in measurement, we opted for a second experimental approach.

As described serveral times along the preceeding text, each output has spectral contributions from sensing and reference waveguides. Therefore, the absorption of the sample can be estimated by comparing (post-processing) the reference and sensing spectral contributions from a single output. Despite this approach prevents us from obtaining the spectroscopic information of the sample's absorption, which is one of the key features of the proposed device, it allowed us to demonstrate indirectly the pursued working principle.

Thus, the spectra from one input to one output shown in Figure 4.6 are then processed. As explained, the values obtained in this graph show the average normalized power measured from the reference (Reference) and sensing contributions (peak values of the pass-bands) for the different cases analysed: no sample on top of the chip (Air), Glycerine and distilled water (DH_2O) samples. From the traces in Fig. 4.6, we obtained the "Reference" value as the average of peak values of pass-bands 1, 3, 5 and 7. in two steps. In a first step, we averaged all the peak values for each pass-band, that is, all corresponding to peak '1', then peak '3' and so on. The four resulting values were averaged in a second step. For the 'Sensing' cases, the peaks 2, 4, 6 and 8 are averaged as in the previous second step. The results are shown in Fig. 4.7.

From Reference – Air values comparison (Figure 4.7), a decrease in power is observed. This is due to the fact that there is great variation in the propagation of light between the two waveguides cross-sections. In the case of the opened waveguide, the propagating mode is more confined than in the reference waveguides, so the propagation loss is greater, as there is a greater interaction between the

Device	W_{io} (μm)	W_{aw} (μm)	d_w (μm)	N_{in}	N_{out}	$\Delta\lambda_{ch}$ (nm)	$\Delta\lambda_{bw}$ (nm)	$\Delta\lambda_{FSR}$ (nm)	N	m	L_f (μm)	ΔL (nm)
AWG	2	1/0.8	3	2	2	3.0	0.75	12.0	22	99	75.508	97.34
IOSS	2	1/0.8	3	2	4	3.0	0.75	12.0	44	105/105	149.507	98.08/ 98.56

Table 4.2: AWG and IOSS devices main design parameters. Abbreviations: W_{io} stands for input/output slab waveguides width, W_{aw} for arrayed waveguides width (1550 nm/1450 nm design), d_w for the distance between input/output waveguides, N_{in} for the number of input waveguides, N_{out} for the number of output waveguides, $\Delta\lambda_{ch}$ for the channel spacing, $\Delta\lambda_{bw}$ for the channel bandwidth, $\Delta\lambda_{FSR}$ for wavelength Free Spectral Range, N for the total number of arrayed waveguides (AWs), m for grating order, L_f for focal length, ΔL for incremental length between consecutive AWs. Note that for IOSS device two values for m and ΔL are given, one for each sub-array.

propagating mode and the irregularities of the waveguide side walls. On the other hand, the transitions between both cross sections are also abrupt, so they will favour the increase of total losses.

In the case of Reference – Glycerine or Reference – DH_2O results, there is still a variation in the propagation of the mode, but it is no as significant as for Reference-Air, since the refractive indexes contrast is lower in both cases. For this same reason, transition losses are also lower. Nevertheless, the obtained power values for Air, Glycerin and DH_2O follow the expected trend taking into account the bulk absorption reported in the literature measured at 1550 nm wavelength: $\alpha_{air} = 0$, $\alpha_{glycerin} = 11.27$ cm^{-1} [104], and $\alpha_{water} = 12.10$ cm^{-1} [103]. Hence, we believe that absorption is the loss coefficient that has more weight in the calculation of total losses.

The aim of this sensor, however, is not to obtain the absolute absorption value of the sample under analysis, but to perform relative measurements to study the concentration of certain analyte contained in the sample. Absolute measurements require a complete characterization of the technology, however, relative measurements to track the evolution of the sample concentration can be performed simply by applying the correct sensing length.

4.2 Refined IOSS designs

From the previous IOSS design, we were able to observe a power variation for water and DH_2O samples. However we observed that the optical coupling uncertainty was larger than the loss change introduced by the analytes. This would also preclude us from measuring a solution of analytes in water, with reduced concentrations. Therefore, the new designs in this section incorporate longer sensing areas. By lengthening l_s, the device foot-print increased considerably, thus further IOSS modifications were required in order to fit the device to the PIC size (11×5.5 μm^2). The revised design parameters are provided in Table 4.2.

The main change with respect to the previous design is the reduction of the

Device Nr.	Name	λ_0 (nm)	Trenched	Sensing window parameters		
				l_s (mm)	W_{win} (μm)	W_{tw} (μm)
1	AWG-NT@1550	1550	✗	0.0	0.0	1.0
2	IOSS-T@1550	1550	✓	5.0	14.0	1.0
3	IOSS-NT@1550	1550	✗	0.0	0.0	1.0
4	IOSS-T@1450	1450	✓	1.8	14.0	0.8
5	IOSS-NT@1450	1450	✗	0.0	0.0	0.8
6	AWG-T@1550	1550	✓	5.0	14.0	1.0
7	AWG-NT@1450	1450	✗	0.0	0.0	0.8
8	AWG-T@1450	1450	✓	1.8	14.0	0.8
9	IOSS-T@1550-wwg0.8	1550	✓	3.5	14.0	0.8

Table 4.3: AWG and IOSS designs descriptions included in the last fabricated run. Abbreviations: l_s and W_{win} stand for the sensing window length and width, respectively, and W_{tw} is the sensing waveguide width.

number of output waveguides by half, which in turn reduces the total number of AWs (N). On the other hand, the channel spacing ($\Delta\lambda_{ch}$) is set to 3.0 nm to keep a similar FSR than in the first AWG and IOSS versions. These changes helped to reduce the size of the devices and fit several device configurations into the MPW chip area. Note than this area restriction is inherent to the use of MPW fab run. If a dedicated run is employed, the constrain in layout area is comparatively very low.

In this design iteration, the layouts have been distributed in two PICs, shown in Figures 4.8 and 4.9. The description of the designed devices can be found in Table 4.3. As can be observed, there are four devices operating at 1550 nm (AWG and IOSS with and without sensing windows) and the same four operating at 1450 nm. The latter were included because the absorption of glycerin and distilled water is higher around 1450 nm, therefore the analysis has been focused on that range. Still, devices centered at 1550 nm are kept as reference designs, since all the technology has been characterized at this wavelength, and as a link to the previous iteration results described in the preceeding section. The nominal waveguide width employed in the designs is $W = 1\mu$m for devices operating at 1550 nm and $W = 0.8\mu$m for devices operating at 1450 nm, maintaining a bend radius of $R = 75$ μm in all cases. An extra IOSS device operating at 1550 is designed, in order to reduce the l_s by decreasing the width of the trenched waveguide (W_{wt}) from 1.0 μm to 0.8 μm.

The absorption loss coefficient for the different waveguides cross-sections and samples was obtained through simulations, employing OptoDesigner mode solver software (Figure 4.10). The simulated values provide directly $\Gamma\alpha_{sample}$, since the interaction of the sample with the evanescent field is already taken into account. The data on the extinction coefficient of the samples were taken from [103, 104]. Propagation losses, together with transitions losses, are estimated to be between 2 – 3 dB/cm, following the preliminary results obtained from previous fabricated run. Alongside the IOSS, MZIs with trenched sections are within the PICs to provide complementary measurements as cross-checks these values. The sensing

length has been set for the most extreme case, i.e. for the sample with the highest absorption (distilled water). For these designs, l_s is defined as the required length to observe a power decay of -6 dB since, for higher than estimated loss values, the signal could be lost completely. The resulting length for each case is specified in Table 4.3. When the design of the sensor is fully optimised, this criterion will vary and the length that gives the greatest sensitivity to the device will be sought.

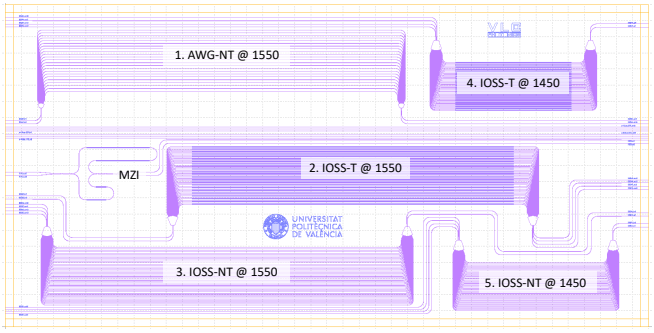

Figure 4.8: Chip layout containing the designs of AWG and IOSS devices centered at 1550 nm without sensing windows (1 and 3), IOSS operating at 1550 nm containing sensing windows (2) and IOSS operating at 1450 nm with (4) and without (5) sensing windows. The MZI placed at the left part of the chip was design to characterize the propagation losses of the trenched waveguides with $W_{wt} = 1.0$.

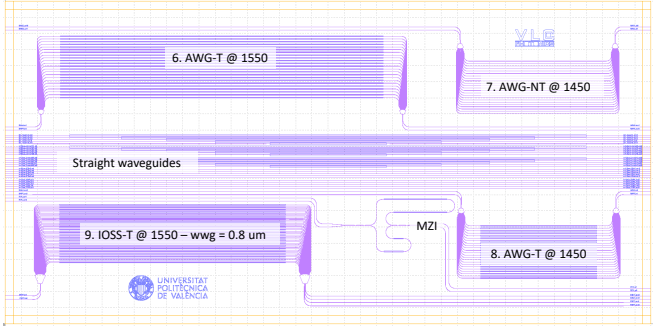

Figure 4.9: Chip layout containing the designs of an AWG operating at 1550 nm containing sensing windows (6), AWGs operating at 1450 nm with (8) and without (7) sensing windows and an IOSS operating at 1550 nm containing sensing windows which waveguides are 0.8 μm width (9). The straight waveguides set and the MZI placed at the lower center part of the chip were design to characterize the propagation losses of the trenched waveguides with $W_{wt} = 0.8$.

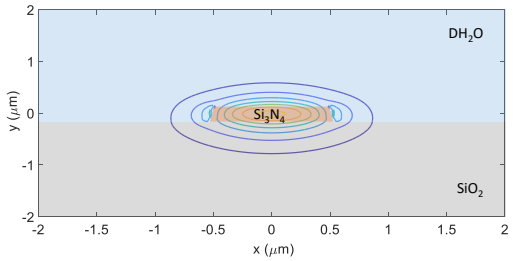

Figure 4.10: Contour plot of the amplitude of the Ex field component of the TE_0 mode of a 1μm wide strip waveguide employed for evanescent sensing.

The simulated response for AWG and IOSS with sensing windows operating at 1450 nm and 1550 nm (devices 2, 4, 6 and 8) are shown in Figure 4.11. As already explained in previous section, no losses are included in the simulations, therefore, the present insertion losses correspond to diffraction losses of the devices. At the time of writing this thesis manuscript, the described designs are being manufactured.

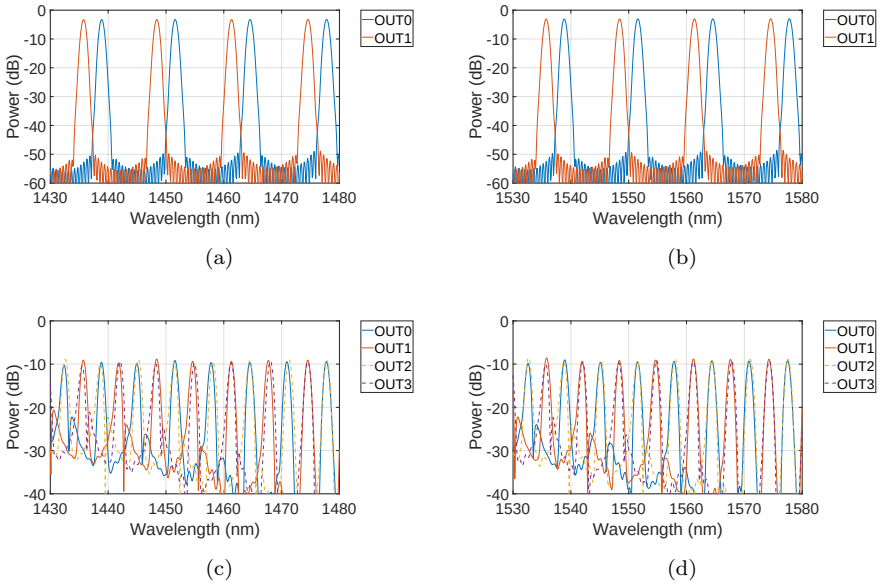

Figure 4.11: Spectral response of (**a**) AWG with trenched waveguide sections operating at 1450 nm, (**b**) AWG with trenched waveguide sections operating at 1550 nm, (**c**) Trenched IOSS operating at 1450 nm, and (**d**) Trenched IOSS operating at 1550 nm simulated response.

4.3 Conclusions

In this chapter we have presented the experimental proof-of-concept for the IOSS device. Several IOSS designs were performed, and some fabricated, allowing to indentifying serveral aspects and means for improvement. They spectral features expected, have been matched, such as de channel spacing, FSR and focal point unfolding, as compared with a regular AWG. In terms of sensing capability, the variation in power of the device response has been observed due to interaction with different samples. However, several practical shortcomings in the first design iteration were identified, and considered in the designs of the second iteration, whose fabrication is on-going at the time of writing. Thus, and despite the experimental validation of this second set is pending, the results from the first designs exhibit sufficient evidence of the intended concept and sensing operation.

Chapter 5
Summary, conclusions and open research lines

5.1 Conclusions

The conclusions drawn from the work elaborated for this Ph.D. are the following:

- Our progress in the development of a moderate confinement silicon nitride platform has been reported in Chapter 2. The characterization of this platform presents propagation properties compatible with the similar existing platforms, despite being developed with fewer process steps. The implementation of extra processes, as the Si_3N_4 oxidation previous cladding deposition, has shown significant improvement regarding propagation losses and dispersion, revealing that there is still room for improvement for this platform. The results obtained from the characterization of this technology demonstrate that this is perfectly useful platform for the development of diverse devices and applications. In addition, this platform is easily accessible through the MPW runs.

- In Chapter 3 the IOSS device concept is presented. The device is based on an AWG where different subsets of arrayed waveguides are defined, and sensing windows (uncovered waveguide sections) are implemented in one (or more) of the subsets. It is, therefore, a compact device capable of performing both spectroscopic and sensing analysis of a sample. The mathematical model to describe IOSS operation and design procedure have been described for its two possible configurations: intensity and frequency/wavelength interrogation. Fur thermore, two reference designs operating at visible and near-infrared wavelength ranges are provided, showing the versatility of the sensor.

- The IOSS experimental proof of concept is reported in Chapter 4. The designed and fabricated device is configured for intensity interrogation. Dif-

ferent configurations of IOSS and AWG are fabricated in the same chip for later comparison. The characterization of the first iteration of the IOSS has yielded good results in terms of channel spacing, FSR and channels duplication. Also from these results, design features to be improved have been observed to mitigate phase errors. The sensing capability could not be fully developed in this first iteration due to space constraints, an issue that has been resolved in the second design. Even so, we have been able to observe a variation in power due to the absorption of different samples. The results obtained from this first proof of concept give us high expectations of achieving the objectives set with the second design.

5.2 Future work

After the work developed in this thesis, there are some open research lines that may be continued:

- Further design optimization of IOSS sensor for intensity interrogation.
- Design and fabrication of IOSS sensor for frequency/wavelength interrogation configuration.
- Implementation of a microfluidic system for continuous solution measurements.
- Study the possible functionalization of the sensor to bring specificity to the analysis.
- Implementation of larger number of sub-arrays for sample multiplexed analysis.

5.3 List of publications

SCI Journal papers

- P. Muñoz, G. Micó, L. A. Bru, D. Pastor, D. Pérez, J. D. Doménech, J. Fernández, R. Baños, B. Gargallo, R. Alemany, A. M. Sánchez, J. M. Cirera, R. Mas and C. Domínguez, "Silicon Nitride Photonc Integration Platforms for Visible, Near-Infrared and Mid-Infrared Applications", *Sensors*, vol. 17, no. 2088, 2017.
- G. Micó, B. Gargallo, D. Pastor, P. Muñoz, "Integrated Optic Sensing Spectrometer: Concept and Design", *Sensors*, vol. 19, no. 1018, 2019.

Conference papers

- G. Micó, D. Pastor, J. D. Doménech, C. Domínguez P. Muñoz,"Ring Resonators and Mach-Zehnder Interferometers based sensors in a Si3N4 technology" *20th Annual Symposium of the IEEE/LEOS Benelux Chapter*, Brussels, Belgium, 26th - 27th November 2015.

- G. Micó, D. Pastor, J. D. Doménech, C. Domínguez P. Muñoz,"Integrated Optical sensors based on a new Si3N4 technology" *XIII European Conference on Optical Chemical Sensors and Biosensors (Europtrode XIII)*, Graz, Austria, 20th - 23rd March 2016.

- G. Micó, L. A. Bru, D. Pastor, D. Pérez, J. D. Doménech, A. M. Sánchez, J. M. Cirera, J. Sánchez, C. Domínguez P. Muñoz,"C-band linear propagation characteristics for a 300 nm film height Silicon Nitride photonics platform" *19th European Conference on Integrated Optics (ECIO)*, Eindhoven, The Netherlands, 3rd - 5th April 2017.

- G. Micó, L. A. Bru, D. Pastor, J. D. Doménech, J. Fernández, A. M. Sánchez, J. M. Cirera, C. Domínguez and P. Muñoz, "Silicon nitride photonics: from visible to mid-infrared wavelengths" *SPIE Photonics West 2018 - Silicon Photonics XIII*, San Francisco, California, United States, February 2018.

- G. Micó, D. Pastor, P. Muñoz, "Optical spectroscopic sensor based on a novel Arrayed Waveguide Grating configuration " *XIV European Conference on Optical Chemical Sensors and Biosensors (Europtrode XIV)*, Naples, Italy, 25th - 28th March, 2018.

- G. Micó, L. A. Bru, D. Pastor, D. Pérez, J. D. Doménech, J. Fernández, R. Baños, B. Gargallo, R. Alemany, A. M. Sánchez, J. M. Cirera, R. Mas, C. Domínguez P. Muñoz, "Silicon nitride photonic integration platform for visible, near-infrared and mid-infrared applications" *XIV European Conference on Optical Chemical Sensors and Biosensors (Europtrode XIV)*, Naples, Italy, 25th - 28th March, 2018.

- G. Micó, L. A. Bru, D. Pastor, J. D. Doménech, A. M. Sánchez, C. Domínguez and P. Muñoz,"Impact of manufacturing processes on the optical amplitude, phase and polarization properties of silicon nitride waveguides" *20th European Conference on Integrated Optics (ECIO)*, Valencia, Spain, 30th May - 1st June 2018.

- G. Micó, B. Gargallo, D. Pastor, P. Muñoz, "Sensor espectroscópico integrado basado en un AWG intercalado" *XI Reunión Española de Optoelectrónica (OPTOEL 2019)*, Zaragoza, Spain, 3rd - 5th July, 2019.

Patents

- P. Muñoz, B. Gargallo, G. Micó, D. Pastor,"Dispositivo Fotónico Sensor, Método de análisis de muestras que hace uso del mismo y usos de dicho dispositivo", ES Patent OEPM P201,631,544.

Bibliography

[1] P. Muñoz, "Photonic integration in the palm of your hand: Generic technology and multi-project wafers, technical roadblocks, challenges and evolution," in *2017 Optical Fiber Communications Conference and Exhibition (OFC)*, pp. 1–3, March 2017.

[2] T. H. Maiman, "Stimulated Optical Radiation in Ruby," *Nature*, vol. 187, pp. 493–494, 1960.

[3] R. P. Riesz, "High speed semiconductor photodiodes," *Review of Scientific Instruments*, vol. 22, no. 994, 1962.

[4] K. C. Kao and G. A. Hockham, "Dielectric-fibre surface waveguides for optical frequencies," *Elektron*, vol. 14, no. 5, pp. 11–12, 1997.

[5] E. MILLER, "THE BELL TECHNICAL SYSTEM Integrated Optics : An Introduction," *THE BELL SYSTEM technical journal*, 1969.

[6] S. Valette, "Integrated Optics : The history and the future," pp. 1–6, 1973.

[7] A. E.-J. Lim, J. Song, Q. Fang, C. Li, X. Tu, N. Duan, K. K. Chen, R. P.-C. Tern, and T.-Y. Liow, "Review of silicon photonics foundry efforts," *IEEE J. Sel. Topics in Quantum Elect.*, vol. 20, no. 4, pp. 405–416, 2014.

[8] M. Smit, X. Leijtens, H. Ambrosius, E. Bente, J. Van der Tol, B. Smalbrugge, T. De Vries, E.-J. Geluk, J. Bolk, R. Van Veldhoven, *et al.*, "An introduction to InP-based generic integration technology," *Semiconductor Science and Technology*, vol. 29, no. 8, p. 083001, 2014.

[9] A. Leinse, R. Heideman, M. Hoekman, F. Schreuder, F. Falke, C. Roeloffzen, L. Zhuang, M. Burla, D. Marpaung, D. Geuzebroek, *et al.*, "TriPleX waveguide platform: low-loss technology over a wide wavelength range," in *Proc. SPIE*, vol. 8767, p. 87670E, 2013.

[10] J. Kischkat, S. Peters, B. Gruska, M. Semtsiv, M. Chashnikova, M. Klinkmüller, O. Fedosenko, S. Machulik, A. Aleksandrova,

G. Monastyrskyi, Y. Flores, and W. Ted Masselink, "Mid-infrared optical properties of thin films of aluminum oxide, titanium dioxide, silicon dioxide, aluminum nitride, and silicon nitride," *Applied Optics*, vol. 51, pp. 6789+, Sept. 2012.

[11] A. Malik, M. Muneeb, Y. Shimura, J. V. Campenhout, R. Loo, and G. Roelkens, "Germanium-on-silicon mid-infrared waveguides and mach-zehnder interferometers," in *2013 IEEE Photonics Conference*, pp. 104–105, Sept 2013.

[12] A. Malik, M. Muneeb, S. Pathak, Y. Shimura, J. V. Campenhout, R. Loo, and G. Roelkens, "Germanium-on-silicon mid-infrared arrayed waveguide grating multiplexers," *IEEE Photonics Technology Letters*, vol. 25, pp. 1805–1808, Sept 2013.

[13] A. Malik, M. Muneeb, Y. Shimura, J. V. Campenhout, R. Loo, and G. Roelkens, "Germanium-on-silicon planar concave grating wavelength (de)multiplexers in the mid-infrared," *Applied Physics Letters*, vol. 103, no. 16, p. 161119, 2013.

[14] L. Shen, N. Healy, C. J. Mitchell, J. S. Penades, M. Nedeljkovic, G. Z. Mashanovich, and A. C. Peacock, "Mid-infrared all-optical modulation in low-loss germanium-on-silicon waveguides," *Opt. Lett.*, vol. 40, pp. 268–271, Jan 2015.

[15] M. Smit, X. Leijtens, H. Ambrosius, E. Bente, J. Van Der Tol, B. Smalbrugge, T. De Vries, E. J. Geluk, J. Bolk, R. Van Veldhoven, L. Augustin, P. Thijs, D. D'Agostino, H. Rabbani, K. Lawniczuk, S. Stopinski, S. Tahvili, A. Corradi, E. Kleijn, D. Dzibrou, M. Felicetti, E. Bitincka, V. Moskalenko, J. Zhao, R. Santos, G. Gilardi, W. Yao, K. Williams, P. Stabile, P. Kuindersma, J. Pello, S. Bhat, Y. Jiao, D. Heiss, G. Roelkens, M. Wale, P. Firth, F. Soares, N. Grote, M. Schell, H. Debregeas, M. Achouche, J. L. Gentner, A. Bakker, T. Korthorst, D. Gallagher, A. Dabbs, A. Melloni, F. Morichetti, D. Melati, A. Wonfor, R. Penty, R. Broeke, B. Musk, and D. Robbins, "An introduction to InP-based generic integration technology," *Semiconductor Science and Technology*, vol. 29, no. 8, 2014.

[16] Y. Akulova, "Indium phosphide photonic integrated circuits," *Encyclopedia of Modern Optics*, vol. 1-5, pp. 242–253, 2018.

[17] https://www.jeppix.eu/mpw-services/get-started/mpw-run-schedule/

[18] https://smartphotonics.nl/our-offering/mpw-runs/

[19] https://europractice-ic.com/wp-content/uploads/2020/05/General-MPW-EUROPRACTICE-200515-v9.pdf

[20] https://photonics.lionix-international.com/mpw-service/

[21] https://www.ligentec.com/ligentec-foundry/

[22] http://www.imb-cnm.csic.es/index.php/en/clean-room/silicon-nitride-technology

[23] M. J. R. Heck, J. F. Bauters, M. L. Davenport, J. K. Doylend, S. Jain, G. Kurczveil, S. Srinivasan, Y. Tang, and J. E. Bowers, "Hybrid silicon photonic integrated circuit technology," *IEEE Journal of Selected Topics in Quantum Electronics*, vol. 19, pp. 6100117–6100117, July 2013.

[24] J. P. Epping, M. Hoekman, R. Mateman, A. Leinse, R. G. Heideman, A. van Rees, P. J. M. van der Slot, C. J. Lee, and K.-J. Boller, "High confinement, high yield Si_3N_4 waveguides for nonlinear optical applications," *Optics Express*, vol. 23, pp. 642+, Jan. 2015.

[25] E. F. Krimmel and R. Hezel, *Si Silicon: Silicon Nitride in Microelectronics and Solar Cells*. Springer-Verlag Berlin Heidelberg, 1991.

[26] W. Stutius and W. Streifer, "Silicon nitride films on silicon for optical waveguides," *Applied Optics*, vol. 16, pp. 3218–3222, Dec. 1977.

[27] R. G. Heideman, R. P. H. Kooyman, and J. Greve, "Performance of a highly sensitive optical waveguide Mach-Zehnder interferometer immunosensor," *Sensors and Actuators B: Chemical*, vol. 10, pp. 209–217, Feb. 1993.

[28] E. F. Schipper, A. M. Brugman, C. Dominguez, L. M. Lechuga, R. P. H. Kooyman, and J. Greve, "The realization of an integrated Mach-Zehnder waveguide immunosensor in silicon technology," *Sensors and Actuators B: Chemical*, vol. 40, pp. 147–153, May 1997.

[29] M. J. Shaw, J. Guo, G. A. Vawter, S. Habermehl, and C. T. Sullivan, "Fabrication techniques for low-loss silicon nitride waveguides," in *Micromachining Technology for Micro-Optics and Nano-Optics III*, vol. 5720, pp. 109–118, 2005.

[30] M. Melchiorri, N. Daldosso, F. Sbrana, L. Pavesi, G. Pucker, C. Kompocholis, P. Bellutti, and A. Lui, "Propagation losses of silicon nitride waveguides in the near-infrared range," *Applied Physics Letters*, vol. 86, pp. 121111+, Mar. 2005.

[31] K. Worhoff, E. Klein, G. Hussein, and A. Driessen, "Silicon oxynitride based photonics," in *2008 10th Anniversary International Conference on Transparent Optical Networks*, vol. 3, pp. 266–269, IEEE, June 2008.

[32] S. C. Mao, S. H. Tao, Y. L. Xu, X. W. Sun, M. B. Yu, G. Q. Lo, and D. L. Kwong, "Low propagation loss SiN optical waveguide prepared by optimal low-hydrogen module," *Optics Express*, vol. 16, pp. 20809+, Dec. 2008.

[33] J. F. Bauters, M. J. R. Heck, D. John, D. Dai, M.-C. Tien, J. S. Barton, A. Leinse, R. G. Heideman, D. J. Blumenthal, and J. E. Bowers, "Ultra-low-loss high-aspect-ratio Si_3N_4 waveguides," *Optics Express*, vol. 19, pp. 3163–3174, Feb. 2011.

[34] J. F. Bauters, M. J. R. Heck, D. D. John, J. S. Barton, C. M. Bruinink, A. Leinse, R. G. Heideman, D. J. Blumenthal, and J. E. Bowers, "Planar waveguides with less than 01 dB/m propagation loss fabricated with wafer bonding," *Optics Express*, vol. 19, pp. 24090–24101, Nov. 2011.

[35] S. Romero-García, F. Merget, F. Zhong, H. Finkelstein, and J. Witzens, "Silicon nitride CMOS-compatible platform for integrated photonics applications at visible wavelengths," *Optics Express*, vol. 21, pp. 14036–14046, June 2013.

[36] A. Z. Subramanian, P. Neutens, A. Dhakal, R. Jansen, T. Claes, X. Rottenberg, F. Peyskens, S. Selvaraja, P. Helin, B. Du Bois, K. Leyssens, S. Severi, P. Deshpande, R. Baets, and P. Van Dorpe, "Low-Loss Singlemode PECVD Silicon Nitride Photonic Wire Waveguides for 532–900 nm Wavelength Window Fabricated Within a CMOS Pilot Line," *IEEE Photonics Journal*, vol. 5, p. 2202809, Dec. 2013.

[37] T. J. Kippenberg, R. Holzwarth, and S. A. Diddams, "Microresonator-Based Optical Frequency Combs," *Science*, vol. 332, pp. 555–559, Apr. 2011.

[38] K. Luke, Y. Okawachi, M. R. E. Lamont, A. L. Gaeta, and M. Lipson, "Broadband mid-infrared frequency comb generation in a Si_3N_4 microresonator," *Optics Letters*, vol. 40, pp. 4823+, Oct. 2015.

[39] C. J. Krückel, A. Fülöp, T. Klintberg, J. Bengtsson, P. A. Andrekson, and V. Torres-Company, "Linear and nonlinear characterization of low-stress high-confinement silicon-rich nitride waveguides," *Optics Express*, vol. 23, pp. 25827+, Sept. 2015.

[40] K. Luke, A. Dutt, C. B. Poitras, and M. Lipson, "Overcoming Si_3N_4 film stress limitations for high quality factor ring resonators," *Optics Express*, vol. 21, pp. 22829–22833, Sept. 2013.

[41] D. Doménech, P. Muñoz, A. Sánchez, J. M. Cirera, and C. Domínguez, "Generic silicon nitride foundry development: Open access to low cost photonic integrated circuits prototyping," in *Opto-electronics Conference (OPTOEL)*, Salamanca (Spain), July 2015.

[42] K. Shang, S. Pathak, B. Guan, G. Liu, and S. J. B. Yoo, "Low-loss compact multilayer silicon nitride platform for 3D photonic integrated circuits," *Optics Express*, vol. 23, pp. 21334+, Aug. 2015.

[43] P. Muellner, A. Maese-Novo, E. Melnik, R. Hainberger, G. Koppitsch, J. Kraft, and G. Meinhardt, "CMOS-compatible low-loss silicon nitride waveguide integration platform for interferometric sensing," in *European Conference on Integrated Optics*, pp. o–19, May 2016.

[44] F. Morichetti, A. Melloni, M. Martinelli, R. G. Heideman, A. Leinse, D. H. Geuzebroek, and A. Borreman, "Box-shaped dielectric waveguides: A new concept in integrated optics?," *J. Lightwave Technol.*, vol. 25, pp. 2579–2589, Sep 2007.

[45] A. Leinse, R. G. Heideman, E. J. Klein, R. Dekker, C. G. H. Roeloffzen, and D. A. I. Marpaung, "Triplex platform technology for photonic integration: Applications from uv through nir to ir," in *2011 ICO International Conference on Information Photonics*, pp. 1–2, May 2011.

[46] L. Zhuang, D. Marpaung, M. Burla, M. Khan, C. Roeloffzen, W. Beeker, A. Leinse, and R. Heideman, "On-chip microwave photonic signal processors in low-loss, high-index-contrast si3n4/sio2 waveguides," *Antennas and Propagation (EuCAP 2011)*, vol. 2774, p. 2778, 2011.

[47] W. D. Sacher, Y. Huang, G.-Q. Lo, and J. K. S. Poon, "Multilayer Silicon Nitride-on-Silicon Integrated Photonic Platforms and Devices," *Journal of Lightwave Technology*, vol. 33, pp. 901–910, Feb. 2015.

[48] X. Ji, F. A. S. Barbosa, S. P. Roberts, A. Dutt, J. Cardenas, Y. Okawachi, A. Bryant, A. L. Gaeta, and M. Lipson, "Ultra-low-loss on-chip resonators with sub-milliwatt parametric oscillation threshold," *Optica*, vol. 4, no. 6, p. 619, 2017.

[49] P. T. Lin, V. Singh, L. Kimerling, and A. M. Agarwal, "Planar silicon nitride mid-infrared devices," *Applied Physics Letters*, vol. 102, pp. 251121+, June 2013.

[50] M. H. P. Pfeiffer, A. Kordts, V. Brasch, M. Zervas, M. Geiselmann, J. D. Jost, and T. J. Kippenberg, "Photonic Damascene process for integrated high-Q microresonator based nonlinear photonics," *Optica*, vol. 3, pp. 20+, Jan. 2016.

[51] Y. Huang, J. Song, X. Luo, T.-Y. Liow, and G.-Q. Lo, "CMOS compatible monolithic multi-layer Si_3N_4-on-SOI platform for low-loss high performance silicon photonics dense integration," *Optics Express*, vol. 22, pp. 21859+, Sept. 2014.

[52] L. Wang, W. Xie, D. Van Thourhout, Y. Zhang, H. Yu, and S. Wang, "Nonlinear silicon nitride waveguides based on PECVD deposition platform," *Optics Express*, vol. 26, no. 8, p. 9645, 2018.

[53] Z. Shao, Y. Chen, H. Chen, Y. Zhang, F. Zhang, J. Jian, Z. Fan, L. Liu, C. Yang, L. Zhou, and S. Yu, "Ultra-low temperature silicon nitride photonic integration platform," *Optics Express*, vol. 24, pp. 1865+, Jan. 2016.

[54] P. T. Lin, V. Singh, H.-Y. G. Lin, T. Tiwald, L. C. Kimerling, and A. M. Agarwal, "Low-Stress Silicon Nitride Platform for Mid-Infrared Broadband and Monolithically Integrated Microphotonics," *Advanced Optical Materials*, vol. 1, pp. 732–739, Oct. 2013.

[55] W. Lukosz and K. Tiefenthaler, "Directional switching in planar waveguides effected by adsorption-desorption processes," in *European Conference on Integrated Optics*, 1983.

[56] R. Narayanaswamy and O. S. Wolfbeis, *Optical Sensors. Industrial Environmental and Diagnostic Applications.* Berlin ; New York : Springer, c2004., 1 ed., 2004.

[57] A. Rahim, E. Ryckeboer, A. Z. Subramanian, S. Clemmen, B. Kuyken, A. Dhakal, A. Raza, A. Hermans, M. Muneeb, S. Dhoore, Y. Li, U. Dave, P. Bienstman, N. Le Thomas, G. Roelkens, D. Van Thourhout, P. Helin, S. Severi, X. Rottenberg, and R. Baets, "Expanding the Silicon Photonics Portfolio with Silicon Nitride Photonic Integrated Circuits," *Journal of Lightwave Technology*, vol. 35, no. 4, pp. 639–649, 2017.

[58] M. A. Porcel, A. Hinojosa, H. Jans, A. Stassen, J. Goyvaerts, D. Geuzebroek, M. Geiselmann, C. Dominguez, and I. Artundo, "Silicon nitride photonic integration for visible light applications," *Optics and Laser Technology*, vol. 112, no. May 2018, pp. 299–306, 2019.

[59] L. Lechuga, *Optical biosensors*, vol. 44. 2005.

[60] W.-K. Kuo, W.-S. Lin, and S.-W. Yang, "Thin-film tunable bandpass filter for spectral shift detection in surface plasmon resonance sensors," *Optics Letters*, vol. 45, no. 1, p. 65, 2020.

[61] B. Chocarro-Ruiz, S. Herranz, A. Fernández Gavela, J. Sanchís, M. Farré, M. P. Marco, and L. M. Lechuga, "Interferometric nanoimmunosensor for label-free and real-time monitoring of Irgarol 1051 in seawater," *Biosensors and Bioelectronics*, vol. 117, no. May, pp. 47–52, 2018.

[62] E. Melnik, F. Strasser, P. Muellner, R. Heer, G. C. Mutinati, G. Koppitsch, P. Lieberzeit, M. Laemmerhofer, and R. Hainberger, "Surface Modification of Integrated Optical MZI Sensor Arrays Using Inkjet Printing Technology," *Procedia Engineering*, vol. 168, pp. 337–340, 2016.

[63] P. Bienstman, S. Werquin, C. Lerma Arce, D. Witters, R. Puers, J. Lammertyn, T. Claes, E. Hallynck, J.-W. Hoste, and D. Martens, "Ring resonator based SOI biosensors," 2013.

[64] J. V. O. Os, J. J. Ramsden, G. Cs, . Ucs, I. Szendr + O D, S. M. De Paul, M. Textor, and N. D. Spencer, "Optical grating coupler biosensors," *Biomaterials*, vol. 23, pp. 3699–3710, 2002.

[65] E. Ryckeboer, X. Nie, A. Dhakal, D. Martens, P. Bienstman, G. Roelkens, and R. Baets, "Spectroscopic sensing and applications in Silicon Photonics," in *IEEE 14th International Conference on Group IV Photonics (GFP)*, pp. 4–5, 2017.

[66] H. Takahashi, S. Suzuki, and I. Nishi, "Wavelength multiplexer based on SiO/sub 2/-Ta/sub 2/O/sub 5/arrayed-waveguide grating," *Journal of Lightwave Technology*, vol. 12, no. 6, pp. 989–995, 1994.

[67] D. Feng, W. Qian, H. Liang, C.-C. Kung, J. Fong, B. J. Luff, and M. Asghari, "Fabrication insensitive echelle grating in silicon-on-insulator platform," *IEEE Photon. Technol. Lett*, vol. 23, no. 5, pp. 284–286, 2011.

[68] P. Muñoz, D. Pastor, and J. Capmany, "Modeling and Design of Arrayed Waveguide Gratings," *J. Lightwave Technol.*, vol. 20, no. 4, p. 661, 2002.

[69] Y. Kodate, K; Komai, "Compact spectroscopic sensor using an arrayed waveguide grating," *Journal of Optics A: Pure and Applied Optics*, vol. 10, p. 044011 (7pp), 2008.

[70] A. Z. Subramanian, E. Ryckeboer, A. Dhakal, F. Peyskens, A. Malik, B. Kuyken, H. Zhao, S. Pathak, A. Ruocco, A. De Groote, P. Wuytens, D. Martens, F. Leo, W. Xie, U. D. Dave, M. Muneeb, P. Van Dorpe, J. Van Campenhout, W. Bogaerts, P. Bienstman, N. Le Thomas, D. Van Thourhout, Z. Hens, G. Roelkens, and R. Baets, "Silicon and silicon nitride photonic circuits for spectroscopic sensing on-a-chip [Invited]," *Photonics Research*, 2015.

[71] H. Zhao, S. Clemmen, A. Raza, and R. Baets, "Stimulated Raman spectroscopy of analytes evanescently probed by a silicon nitride photonic integrated waveguide," *Optics Letters*, vol. 43, no. 6, pp. 1403–1406, 2018.

[72] A. Vasiliev, M. Muneeb, and J. Allaert, "Integrated Silicon-on-Insulator Spectrometer With Single Pixel Readout for Mid-Infrared Spectroscopy," *IEEE Journal of Selected Topics in Quantum Electronics*, vol. 24, no. 6, 2018.

[73] E. Ryckeboer, R. Bockstaele, M. Vanslembrouck, and R. Baets, "Glucose sensing by waveguide-based absorption spectroscopy on a silicon chip," *Biomedical Optics Express*, vol. 5, no. 5, pp. 12356–12364, 2014.

[74] C. R. Doerr, "Proposed {WDM} cross connect using a planar arrangement of waveguide grating routers and phase shifters," *IEEE Photonics Technology Letters*, vol. 10, no. 4, pp. 528–530, 1998.

[75] C. R. Doerr, L. Zhang, and P. J. Winzer, "Monolithic InP Multiwavelength Coherent Receiver Using a Chirped Arrayed Waveguide Grating," *J. Lightwave Technol.*, vol. 29, pp. 536–541, feb 2011.

[76] B. Gargallo and P. Muñoz, "Full field model for interleave-chirped arrayed waveguide gratings," *Optics express*, vol. 21, no. 6, pp. 6928–6942, 2013.

[77] Y. Okawachi, K. Saha, J. S. Levy, Y. H. Wen, M. Lipson, and A. L. Gaeta, "Octave-spanning frequency comb generation in a silicon nitride chip," *Optics Letters*, vol. 36, pp. 3398–3400, Aug. 2011.

[78] D. J. Moss, R. Morandotti, A. L. Gaeta, and M. Lipson, "New CMOS-compatible platforms based on silicon nitride and Hydex for nonlinear optics," *Nature Photonics*, vol. 7, pp. 597–607, July 2013.

[79] J. P. Epping, T. Hellwig, M. Hoekman, R. Mateman, A. Leinse, R. G. Heideman, A. van Rees, P. J. van der Slot, C. J. Lee, C. Fallnich, and K.-J. Boller, "On-chip visible-to-infrared supercontinuum generation with more than 495 thz spectral bandwidth," *Opt. Express*, vol. 23, pp. 19596–19604, Jul 2015.

[80] H. Zhao, B. Kuyken, S. Clemmen, F. Leo, A. Subramanian, A. Dhakal, P. Helin, S. Severi, E. Brainis, G. Roelkens, and R. Baets, "Visible-to-near-infrared octave spanning supercontinuum generation in a silicon nitride waveguide," *Optics Letters*, vol. 40, pp. 2177+, May 2015.

[81] A. Kordts, M. H. P. Pfeiffer, H. Guo, V. Brasch, and T. J. Kippenberg, "Higher order mode suppression in high-q anomalous dispersion sin microresonators for temporal dissipative kerr soliton formation," *Opt. Lett.*, vol. 41, pp. 452–455, Feb 2016.

[82] P. Muñoz, P. W. Van Dijk, D. Geuzebroek, M. Geiselmann, C. Dominguez, A. Stassen, J. D. Domenech, M. Zervas, A. Leinse, C. G. Roeloffzen, B. Gargallo, R. Banos, J. Fernandez, G. M. Cabanes, L. A. Bru, and D. Pastor, "Foundry Developments Toward Silicon Nitride Photonics from Visible to the Mid-Infrared," *IEEE Journal of Selected Topics in Quantum Electronics*, vol. 25, no. 5, 2019.

[83] J. Maldonado, A. B. González-Guerrero, C. Domínguez, and L. M. Lechuga, "Label-free bimodal waveguide immunosensor for rapid diagnosis of bacterial infections in cirrhotic patients," *Biosensors and Bioelectronics*, vol. 85, pp. 310–316, 2016.

[84] "Photonic integrated circuits design software." www.synopsys.com.

[85] U. Glombitza and E. Brinkmeyer, "Coherent frequency-domain reflectometry for characterization of single-mode integrated-optical waveguides," *Journal of Lightwave Technology*, vol. 11, pp. 1377–1384, Aug 1993.

[86] B. J. Soller, D. K. Gifford, M. S. Wolfe, and M. E. Froggatt, "High resolution optical frequency domain reflectometry for characterization of components and assemblies," *Opt. Express*, vol. 13, pp. 666–674, Jan 2005.

[87] D. K. Gifford, B. J. Soller, M. S. Wolfe, and M. E. Froggatt, "Optical vector network analyzer for single-scan measurements of loss, group delay, and polarization mode dispersion," *Appl. Opt.*, vol. 44, pp. 7282–7286, Dec 2005.

[88] L. A. Bru, D. Pastor, and P. Muñoz, "Integrated optical frequency domain reflectometry device for characterization of complex integrated devices," *Optics Express*, vol. 26, no. 23, p. 30000, 2018.

[89] P. Muñoz, G. Micó, L. A. Bru, D. Pastor, D. Pérez, J. D. Doménech, J. Fernández, R. Baños, B. Gargallo, R. Alemany, A. M. Sánchez, J. M. Cirera, R. Mas, and C. Domínguez, "Silicon nitride photonic integration platforms for visible, near-infrared and mid-infrared applications," *Sensors*, vol. 17, no. 9, 2017.

[90] M. A. Tran, T. Komljenovic, J. C. Hulme, M. L. Davenport, and J. E. Bowers, "A robust method for characterization of optical waveguides and couplers," *IEEE Photonics Technology Letters*, vol. 28, pp. 1517–1520, July 2016.

[91] M. K. Smit and C. van Dam, "PHASAR-Based WDM-Devices: Principles, Design and Applications," *IEEE Journal of Selected Topics in Quantum Electronics*, vol. 2, no. 2, pp. 236–250, 1996.

[92] E. Kleijn, M. K. Smit, X. J. M. Leijtens, S. Member, and A. M. Profile, "New Analytical Arrayed Waveguide Grating Model," vol. 31, no. 20, pp. 3309–3314, 2013.

[93] J. Goodman, *Introduction to Fourier optics*. 2005.

[94] P. Muñoz, D. Pastor, J. Capmany, and A. Martínez, "Geometrical optimization of the transmission and dispersion properties of arrayed waveguide gratings using two stigmatic point mountings," *Opt. Express*, vol. 11, pp. 2425–2432, sep 2003.

[95] T. P. Coultate, *Food: the chemistry of its components*, ch. 6, pp. 214–267. Royal Society of Chemistry, 2009.

[96] V. R. Horowitz, L. A. Janowitz, A. L. Modic, P. A. Heiney, and P. J. Collings, "Aggregation behavior and chromonic liquid crystal properties of an anionic monoazo dye," *Physical Review E*, vol. 72, no. 4, p. 41710, 2005.

[97] J. Jiménez-Márquez, F. and Vázqueza, J. Úbedab, J. Rodríguez-Reya, and J. L. Sánchez-Rojasa, "Optoelectronic sensor device for monitoring ethanol concentration in winemaking applications," in *Proc. of SPIE Vol. 9517 95171P-1*, p. 10, 2015.

[98] N. Kakuta, H. Yamashita, D. Kawashima, K. Kondo, H. Arimoto, and Y. Yamada, "Simultaneous imaging of temperature and concentration of ethanol-water mixtures in microchannel using near-infrared dual-wavelength absorption technique," *Measurement Science and Technology*, vol. 27, no. 11, p. 12, 2016.

[99] J. Zou, Z. Le, J. Hu, and J.-J. He, "Performance improvement for silicon-based arrayed waveguide grating router," *Optics Express*, vol. 25, no. 9, p. 9963, 2017.

[100] N. Ismail, F. Sun, G. Sengo, K. Wörhoff, A. Driessen, R. M. de Ridder, and M. Pollnau, "Improved arrayed-waveguide-grating layout avoiding systematic phase errors," *Optics Express*, vol. 19, no. 9, p. 8781, 2011.

[101] Z. Zhang, Y. Wang, and H. K. Tsang, "Experimental study of dependence of waveguide array phase errors on waveguide width," *Optics InfoBase Conference Papers*, vol. Part F138-ACPC 2019, pp. 2019–2021, 2019.

[102] E. Kleijn, P. J. Williams, N. D. Whitbread, M. J. Wale, M. K. Smit, and X. J. Leijtens, "Sidelobes caused by polarization rotation in arrayed waveguide gratings," *2011 ICO International Conference on Information Photonics, IP 2011*, vol. 20, no. 20, pp. 1662–1664, 2011.

[103] S. Kedenburg, M. Vieweg, T. Gissibl, and H. Giessen, "Linear refractive index and absorption measurements of nonlinear optical liquids in the visible and near-infrared spectral region," *Optical Materials Express*, vol. 2, no. 11, p. 1588, 2012.

[104] K. Wang, W. Wen, Y. Wang, K. Wang, J. He, J. Wang, P. Zhai, Y. Yang, and P. Qiu, "Order-of-magnitude multiphoton signal enhancement based on characterization of absorption spectra of immersion oils at the 1700-nm window," *Optics Express*, vol. 25, no. 6, p. 5909, 2017.